UNIVERSITY OF HAMBURG

Fachbereich Geowissenschaften, Mineralogisch-Petrographisches (MPI)

Pressure-induced structural changes in metamict zircon

MASTER THESIS

Felipe Andres Pina Binvignat

07.04.2015

Erstgutachter: PD Dr. Boriana Mihailova

Zweitgutsachter: Prof. Dr. Ulrich Bismayer

Contents

Abstract

In-situ high pressure Raman spectroscopy and complementary X-ray diffraction and electron microprobe analysis at ambient conditions are studied by metamict minerals which contain radioactive elements as substitutional point defects and exhibit a complex structure state consisting of the coexistence of crystalline nanoregions with defects and amorphous nanoregions due to the radioactive self-irradiation. This study deals with the structural alteration the metamict mineral zircon (nominal formula $ZrSiO_4$) under pressure up to 10 GPa. It investigates the structural difference between weakly, moderately and heavily metamict zircon at ambient conditions as well as the stability of the zircon structure under high pressure. The study aimed to shed light on the question why a natural mineral like zircon, which contains radioactive elements in its structure, can maintain its stability over millions of years and how we can use this knowledge for the immobilization of nuclear waste products. The zircon samples studied here are from the collection of the Mineralogical Museum of the University of Hamburg and originate from Sri Lanka and Laos. All samples were measured by electron microprobe analysis to verify the chemical homogeneity and to determine the chemical composition and the consequently radioactive dose. The weakly and moderately metamict zircon samples were probed by powder X-ray diffraction at ambient pressure condition to determine the average size of the crystalline nanoregions. In-situ high-pressure Raman spectroscopy was applied to follow the pressure evolution of the structure up to 10 GPa. This method allows to clearly distinguish between signals from the crystalline and amorphous fraction and thus to follow the pressure-induced changes in both crystalline and amorphous nanoregions. Thorough analyses of the pressure evolution of the wavenumbers and the full width at half maximum (FWHM) for selected crystalline and amorphous Raman peaks arising from internal and external SiO_4 modes has been performed. Using the Raman data the local compressibilities of primary sturctural units in metamict zircons with different degree of radiation-induced structural damage could be compared on the basis of the pressure dependencies of the wavenumbers. It is shown that the compressibility of crystalline nanoregions increases with the radiation dose i.e. the stiffness decreases, due to the presence of structural defects. The compressibility of the amorphous nanoregions does not depend on the radiation dose. However the amorphous fraction increases with the radiation dose as revealed by the relative integrated intensities of the Raman peaks originated from the amorphous and the crystalline fraction. Within

uncertainties, the amorphous fraction relative to the crystalline fraction does not change with pressure. However the pressure dependence of the Raman peak positions and widths reveal that both the crystalline and amorphous regions undergo structural alteration between 3 and 6 GPa, consisting of a weakening of the Si-O bond strength in the amorphous regions accompanied by a damping of the SiO_4 stretching in the crystalline region. The former is most probably due to the increase in the Si coordination from 4 to 5 or 6 as theoretically predicted by Trachenko [1], whereas the latter indicates instability in the crystalline region. The Raman analyses of several spatial regions from the same sample indicate that for heavily metamict zircon there are two pathways for the structure to adapt to high pressure: by changing the Si-coordination in the amorphous regions or by structural alterations in both crystalline and amorphous regions. In either case the overall average structure softens between 3 and 6 GPa. Measurements on decompression show that the pressure induced structural changes are not entirely reversible.

1. Introduction

Zircon has a major influence in mineralogy and geochemistry. Its chemical and physical properties to incorporate and retain trace elements are largely determined by its crystalline structure. This is useful for studying the evolution of the Earth crust and mantel [2] as well for age dating [3]. Zircon is also considered to be the oldest mineral in the world. Its property to contain and maintain radioactive elements like Th or U on the geological time scale makes it of interest to seal nuclear waste [4].

The natural process of radioactive decay of U or Th destroys the periodic crystalline structure in zircon. This process is named metamictization. During the radioactive decay highly energetic α-particles are emitted. The α-particles are He^{2+} ions, composed of two neutrons and two protons. Due to recoil processes of the heavy nucleus the crystalline structure is destroyed. High kinetic energy α-particles can break the bonds between the nearest atoms in the crystal. The radiation-induced knock-on effect of nuclei can lead to amorphous regions in the mineral. As a result the mineral loses its structural homogeneity and its density decreases. The long range order in these regions can be lost, which enhances the possibility for chemical transport. The metamictization process can therefore transform an originally crystalline mineral to an amorphous matrix while keeping its idiomorphic shape. Metamict minerals are therefore structural model systems for studying the long-term elastic stability of matrices with actinide-bearing radioactive elements.

1.1 Metamict minerals

Examples for metamict minerals are zircon, pyrochlore, titanite, thorite, brannerite and chevkinite [5]. Metamict minerals can substitute some of its constituents with radioactive elements like U or Th. Through the natural process of α-decay, such elements destroy the crystalline structure and create partially or entirely disordered spatial regions in the host. Two processes occur during the α-decay event. A heavy α-recoil nucleus with low energy is released, which converts its energy in elastic collision over a very short range. In addition a light α-particle (He nucleus) with high energy creates a few hundred isolated atomic displacement tracks in the crystalline matrix (Fig. 1). The long range order in these regions is hence lost. The mass density of the metamict mineral decreases and enhances the possibility for chemical transport. A consequence of the self-irradiation is the unique microstructure called metamict state: coexistences of amorphous and crystalline nano-regions with defects. Heavily metamict minerals, which have experienced large doses of self-irradiation, may become completely amorphous. The metamictization process transforms the crystalline zircon with a few isolated defects into an amorphous matrix with a few isolated nanocrystals. This explains the absence of Bragg peaks in heavy metamict minerals. The macroscopic crystal shape remains unchanged. High temperatures can cause metamict minerals to recrystallize. In particular for zircon the recrystallization can be enhanced if it contains traces of, water respectively OH groups [4].

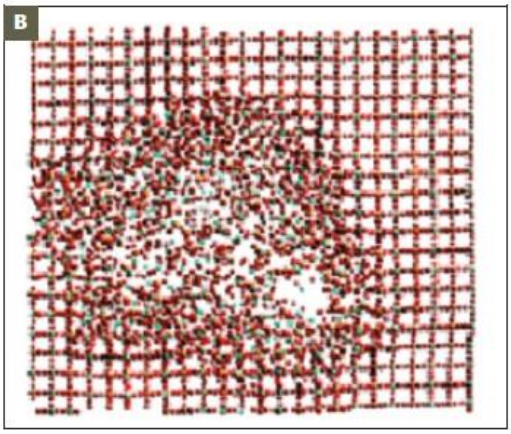

Fig. 1: Simulation of the metamict state. Zircon atoms are blue, silicon atoms yellow and oxygen atoms red. [6]

1.2 The structure of zircon and related minerals

Zircon is an orthosilicate with tetragonal space group $I4_1/amd$. The general formula of zircon is ATO_4. A and T are cations which can be substituted. The A site can be occupied by Zr, Hf, Th, U and Y, where the T site can be occupied by Si ,P ,Cr, As and V (see Fig. 2). Hafnon ($HfSiO_4$), coffinite ($USiO_4$), thorite ($ThSiO_4$) and xenotime (YPO_4) are examples for minerals with the same general formula of ATO_4 but with different chemical compounds.

Hafnon ($HfSiO_4$) has an almost identical structure compared to zircon except for a small difference in the bond length and angles. The ionic radius of Hf^{4+} is 0.83 Å and for Zr^{4+} is 0.84 Å. [7]. Crystalline zircon contains often less than 3 wt % of Hf, with concentrations varying between 0.5 and 7 wt % Hf. Coffinite ($USiO_4$) is one of three naturally occurring ATO_4 actinide silicates. Two of them are identical with zircon, coffinite ($USiO_4$) and thorite ($ThSiO_4$). Coffinite ($USiO_4$) appears in nature as a microscopic intergrowth which is unsuitable for structure determination by conventional X-ray diffraction methods and hydrothermal syntheses produces only a fine-grained powder [8]. The structural relation between zircon and coffinite was identified by X-ray diffraction of synthetic coffinite [9]. Xenotime (YPO_4) is a naturally occurring rare earth element (REE) phosphate which crystallizes with zircon structure. It is topologically identical to other zircon-orthophosphates, with REE^{3+} ions occupying Zr-equivalent dodecahedral sites and P^{5+}occupying Si-equivalent tetrahedral sites [10].

Zircon has isolated SiO_4 tetrahedra which share corners and edges with ZrO_8 dodecahedra (Fig. 2). ZrO_8 shares edges with each other parallel <100>. The bonds of the ZrO_8 dodecahedra are extended in c direction and compressed in a and b direction. (Fig. 3a). Zr and Si also form an edge connection of alternating ZrO_8 and SiO_4 parallel to [001] (Fig. 3b). ZrO_8 dodecahedra share four edges with adjacent ZrO_8 dodecahedra. Two of them in each equivalent crystallographic direction, [100] and [010] [11]. There are small voids between SiO_4 and ZrO_8 polyhedra and open channels parallel to [001]. These voids are proposed to incorporate radioactive impurities, provided that such interstitial sites can accommodate such large ions without excessive structural strain [7]. Metamictization experiments performed for neptunite, titanite, gadolinite, zircon and olivine showed that if there are more different chemical components are part of the structure, the critical metamictization dose gets lower [12].

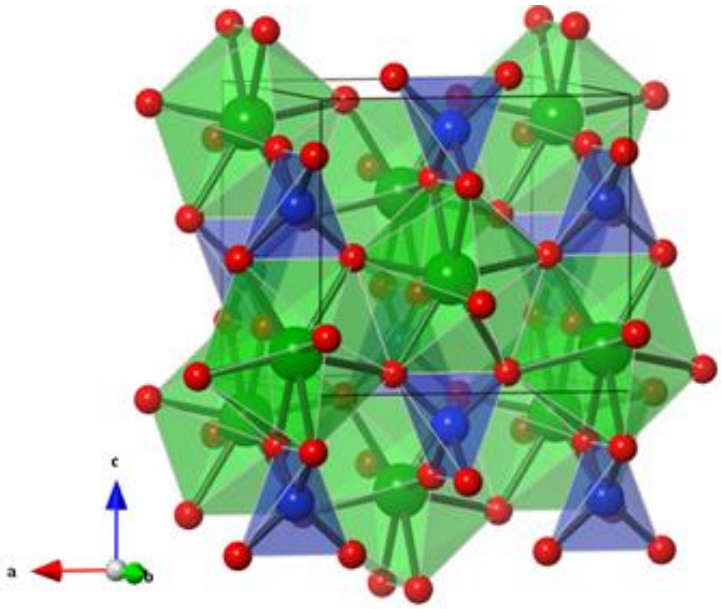

Fig. 2: Structure of zircon in b direction. Green polyhedra are ZrO_8 (A position), blue tetrahedra are SiO_4 (T position) and red spheres are O.

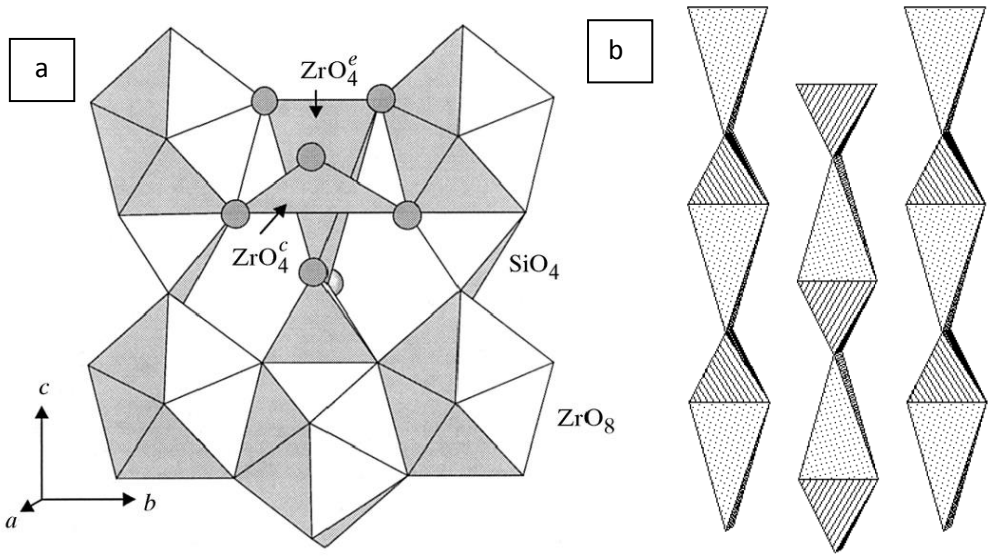

Fig. 3: **3a**. View of zircon structure projected onto (100) [13]. ZrO_8 dodecahedra are crossed linked by edges with SiO_4 tetrahedra. The bonds of the ZrO_8 dodecahedra are extended the along c direction and compressed in a- and b-direction. **3b.** Zircon structure projected on (100), *c* axis is vertical and *b* axis horizontal. Alternating ZrO_8 (light striped) and SiO_4 (dark striped) polyhedra are parallel to [001] [11].

1.3 Previous high pressure studies

The analysis of the structural stability of metamict minerals requires to study the structural state also under non-ambient conditions. There are numerous studies dedicated to temperature induced structural transformation in zircon. Only few analyses of the structures under high pressure have been reported so far. Knittle and Williams have studied pure zircon by high-pressure Raman spectroscopy and X-ray diffraction (XRD) up to 37 GPa. At 23 ± 1 GPa and 300K, $ZrSiO_4$ undergoes a first-order phase transition, from zircon- to the scheelite-type structure. [14] The phase transformation is irreversible. On decompression at ambient pressure the scheelite structure is quenchable. X-ray diffraction analysis of $ZrSiO_4$ with scheelite structure yield lattice parameters of a = 4.726(12) Å and c = 10.515(44) Å which are in excellent agreement with those of $ZrSiO_4$ (scheelite structure) formed under simultaneous high-pressure and high-temperature conditions. The results support a martensitic-type mechanism for the transition from the zircon structure to scheelite structure proposed to explain the shock-induced phase transformation in $ZrSiO_4$. Other compounds with the general formula AXO_4 also exhibit a pressure-induced phase transition from a zircon-($I4_1/amd$) to a sheelite-type ($I4_1/a$) structure [15].

Trachenko studied the response of radiation-damaged zircon under high pressure by measuring the pressure-dependence of the volume using the precise strain-gauge technique and performing complementary molecular-dynamics simulations. The authors used metamict zircon amorphized by natural radiation over geologic times. Increasing the pressure in zircon leads to its softening beginning near 4 GPa. Molecular-dynamics simulations revealed that this softening is associated with an amorphous-amorphous transition accompanied by an increase of the local coordination. The authors observed permanent densification of the quenched sample under high temperatures and a pressure between 4.5 GPa to 9 GPa. These features point to a new class of amorphous materials that shows a response to pressure which is clearly different from that of crystals [1].

In-situ high-pressure single-crystal X-ray diffraction of heavily metamict zircon (amorphous fraction between 65 and 85%) were conducted by Ríos at room temperature and revealed two structural states. From ambient pressure to 3 GPa the diffraction maxima did not show significant changes. However between 3 GPa and 7 GPa a simultaneous increase in peak intensity and decrease in mosaic spread was observed. These effects were attributed to reorientations of crystalline domains within the amorphous matrix. Decompression experiments showed that the structural changes taking place above 3 GPa are reversible [16].

Nasdala [17] studied pressure-induced structural changes up to 10 GPa using Raman spectroscopy, in four natural gem-quality zircon samples with different degrees of self-irradiation damage as well as synthetic zircon without radiation damage. On increasing pressure radiation-damaged zircon shows shifts to higher wavenumbers of the internal SiO_4 stretching modes similar to non-damaged zircon. Some changes in the widths of the Raman peaks were observed in all zircons. This makes it possible to estimate the degree of radiation damage of zircon inclusions in situ from the width of the anti-symmetrical stretching of SiO_4 tetrahedra band and almost independent from potential ‘‘fossilized pressures’’ or compressive strain acting on the inclusions. No spectroscopic evidences for amorphous-amorphous transformations were found by Nasdala [17] .It should be noted that Nasdala have focused mainly on the analysis of the internal SiO_4 tetrahedral modes and did not study the Raman scattering in the low-energy range, which is usually most informative of structural transformations. [17].

The present study concerns with pressure-induced phenomena in metamict zircon under conditions of up to 10 GPa. It includes the differences of crystalline- and metamict zircon at ambient- and high-pressure, structural changes and chemical composition. The aim of this study is to better understand the high stability of a natural mineral like zircon which maintains itself over millions of years, even including radioactive elements in its structure. The better understanding of metamict minerals should improve our knowledge for sealing atomic waste in an appropriate way.

2. Experimental

2.1 Samples

Number of Sample	density (g/cm^3)	Age (Ma)	Locality
Z7	4.675	254±1	1 km north of Bo-Ko-Noi, Mongka, Indochina
Z1	4.583	570±40	Sri Lanka
Z3	4.209	570±40	Sri Lanka
Z4	4.132	570±40	Sri Lanka

Table. 1: Summarize the most important information about in this used Study.

Zircon samples studied here are from the Mineralogical Museum of the University of Hamburg. All samples were analyzed using electron microprobe and Raman spectroscopy at ambient pressure (Table.1). Sample Z7 and a sample with a density to represent an intermediate state similar to Z1were measured at ambient pressure by powder diffraction. An additional sample studied here is from Ceylon (Sri Lanka). The samples Z1 to Z4 are of gem stone quality. Zircons of Sri Lanka are supposed to be 570 ± 40 Ma old [18]. Sample Z7 is from Mongka, Indochina. Mongka is the native name of the corresponding district [19]. It is located between the rivers Megok, Sésan and Srepok. Today it is southwest of Laos at the border to Cambodia [19]. Zircon Z7 is dated 254 ± 1 Ma [20, 21].

2.2 X-ray diffraction

X-rays were discovered in 1896 by Röntgen. X-rays are electromagnetic waves with a wavelength between $0.25 \cdot 10^{-8}$ m and 10^{-12} m. Such wavelengths are placed between the ultraviolet region and the region of γ-rays emitted by radioactive substances. The electric and the magnetic field vector are orthogonal to the direction of the propagation direction of the wave. The typical range of wavelengths from 0.4 Å to 2.5 Å is particularly important for crystallography, because it corresponds to the interatomic distances in crystals. When X-rays interact with matter several processes can happen. Photons of the incident beam are deflected without change of the wavelength (elastic scattering). Other photons lose energy by scattering or scatter with even more energy than before interacting with matter (inelastic scattering). The photons can also be absorbed by atoms (X-ray absorption).

This leads to the exaltation or removal of some inner-shell electrons. Subsequent transition of higher energy level electron to the vacant core levels emits photons with the characteristic wavelength of the atom [22].

Elastically deflected X-rays by the lattice planes, with interplanar distances d_{hkl} form a diffraction pattern. Constructive interference (Fig. 4) is described by the Bragg equation:

$$2 \cdot sin\theta = \frac{n \cdot \lambda}{d_{hkl}}$$, where

θ: is the Bragg angle

λ: is the Wavelength of the incident X-ray

n: is Integer

d_{hkl}: distance between lattice planes

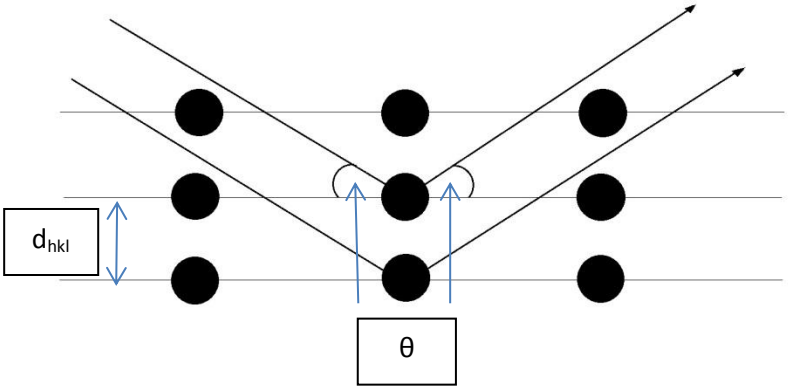

Fig. 4: X-ray deflected on reciprocal lattice planes

As a result of the X-ray diffraction a typical pattern is created, carrying information about the structure, lattice parameters, crystallite size and possible elastic strain and/or defects. The peak position and intensity of the pattern contain information to identify the material symmetry, structure and lattice parameter. The full width at half maximum (FWHM) includes information about the crystallite size (using Scherrer equation), strain (shifted peak position by uniform strain and change in the FWHM by non-uniform strain) and defects. The Bragg intensity of powder XRD pattern may be influenced by the preferred particle orientation. The background contains information about the amorphous content of the sample and the peak tails to defects and diffuse scattering.

In this study a Phillips X-Pert X-ray-powder diffractometer was used with a secondary graphite crystal monochromator, equipped with a point detector and a Cu X-ray tube operating at 40 keV and 30 mA with $K\alpha_1$– and $K\alpha_2$–lines of 1.54059 Å and 1.54443 Å, respectively (Fig. 5). It had a Ni filter to minimize K_β radiation. The secondary monochromator was behind the sample to have better 2theta resolution and only Kα radiation for the detector. An automatic divergence aperture was used to have a constant beam on the sample. The powder XRD patterns were collected in the two-theta range 10 - 85° degree with

a step of 0.02° and accumulation time of 10 s per step. The measurements were performed at ambient pressure and room temperature.

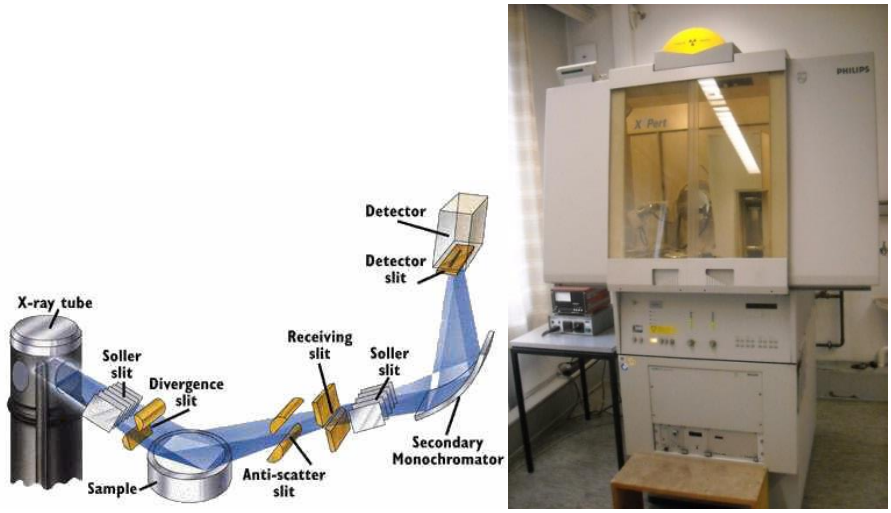

Fig.5: Sketch of the scattering geometry used in XRD experiments [23] and a foto of the X-Pert diffractometer used.

2.3 Electron microprobe analysis

The electron microprobe analysis (EMPA) is based the interaction of an electron beam with the sample and can identify and measure the concentration of elements in micrometer-scale sample volumes. This method allows to quantitatively determine all elements heavier than boron. A focused electron beam interacts with the sample to generate back-scattered electrons (BSE), secondary electrons (SE), characteristic X-rays and cathodoluminescence (CL) (Fig.6). By scanning the surface of the sample with the electron beam, the signals can be used to obtain high resolution scanning electron images (to sub µm resolution), X-ray maps showing the spatial distribution of elements, and CL images for phase (compound and element) identification, estimation of phase distribution and proportions, trace element compositional variation and surface textural analysis of multi-phase composites (EBSD). Characteristic X-rays generated from a microscopic volume in spot mode are utilized to obtain a complete quantitative chemical analysis. The sample has to have a well-polished surface, for accurate quantitative analysis. The range to detected elements was between 100 and 1000 ppm [24].

Fig. 6: Schematic picture of an EMPA [25] and a foto of Cameca electron probe micro-analyzer SX 100

A Cameca electron probe micro-analyzer SX 100 was used for this study (Fig.6). The cathode voltage was 15 keV and the anode current was 40 nA. The emitted X-ray lines from the samples were quantitatively compared with the following 11 synthetic standards: *Al from* Al_2O_3*, Si, Zr from* $ZrSiO_4$*, Mn* from $MnTiO_3$*, Y* from Y_2O_3*, La* from *ree*3, Ce* from *ree2, Nd* from *ree4, Gd* from Gd_2O_3*, Pb* from *Pb-Glas, U* from UO_2 and *Th from Th-glas.*
3 natural standards were: *P* from *apatite, Ca* and *Fe* from *andradit* and *Hf* from *Hf.*

2.4 Raman spectroscopy

Raman spectroscopy is a non-destructive method to study the chemical bonding and structure of solids as well as molecules of fluids or gases using the interaction between visible or near-visible light and atomic vibrations. Raman spectroscopy is based on the Raman effect, which was discovered in 1928 by C.V. Raman and K.S. Krishnan and almost at the same time by G. Landsberg and L.I. Mandelstam. The effect had been theoretically predicted in 1923 by A. Smekal. It was experimentally proven for crystals by G. Landsberg and L.I. Mandelstam and for gases and liquids by C.V. Raman and K.S. Krishnan. 1930 C.V. Raman received the Nobel Prize for his work and the phenomenon was named after him.

The Raman effect is inelastic scattering of light by atomic vibrations (phonon in crystals). The sample is irradiated through an intense laser beam in the near-infrared, visible or ultraviolet region. Usually visible lasers are used, which consist of electromagnetic waves with a single wavelength in the range from 400 to 700 nm. The electromagnetic wave consists of electric and magnetic field components which oscillate in phase perpendicular to each other and perpendicular to the direction of energy propagation. The wavelength λ is defined by the shortest distance between two sequent points oscillating in phase of a wave

function. It can also be described as the relation between the speed of light in vacuum c and the frequency v, describing the number of oscillations per second:

$$\lambda = \frac{c}{v}$$

In vibrational spectroscopy, the frequency is commonly given in wavenumbers $\tilde{v}$ (cm^{-1}), inversely related to the wavelength λ. In contrast to the wavelength the wavenumber is proportional to energy.

$$\tilde{v} = \frac{1}{\lambda} = \frac{v}{c}$$

The quantum of electromagnetic radiation is represented by a particle named photon. The energy of a photon is given by:

$$E = \hbar \cdot \omega$$

ω is the angular frequency and defined by $\omega = 2\pi \cdot v$. Photons interact with matter in terms of transmission, absorption or scattering. They are capable of interacting with atomic vibrations thus they carry information about the properties of matter. The atomic vibrations in a crystal lattice can be described as superposition of its normal vibrational modes. In terms of group theory these normal vibrational modes that can be considered as irreducible representations strictly related to the crystal symmetry. Every atom in a crystal unit cell can vibrate in three dimensions. Due to this, the number of normal vibrations modes is related to the number of atoms and the degrees of freedom of each of those is given by 3·N. The energy of lattice vibrations is quantized and the quantum of lattice vibration is named phonon. The phonon density of states is the complete set of phonon-branches within the first Brillouin zone (FBZ). The FBZ is the Wigner-Seitz cell of the reciprocal space. Those phonon-branches describe the dispersion in the whole FBZ or can be considered as the angular frequency as a function of the wavevektor $\vec{k}$.

In general there are two to types of phonon modes:

Acoustic modes,

In which the participating atoms move in phase and behave like sound waves. In three dimensional crystals there are always 3 acoustic modes. Those modes define the velocity of

sound in a crystal. The acoustic modes do not generate an electrical dipole during the atomic vibrations and therefore they do not interact directly with the electric field of the light.

Optical modes

In the case of optical phonons the atoms move out of phase, inducing a dipole moment. The induced dipole moment can be directly related to the change in the center of gravity of negatively and positively charged ions (for example in the case of infrared-active modes) or it can arise from the modulation of the negatively charged electron shell around the vibrating positively charged nucleus (the case of Raman active modes). The basis consists of atoms, where 3N - 3 phonon modes are optical modes.

The acoustic and optical phonon modes have a different dispersion through the Brillouin zone (Fig. 7). Figure 7 shows the dispersion of a diatomic, one-dimensional chain. The upper (optical) band has comparable small dispersion, throughout the FBZ with zero-frequency for the center ($\vec{k}$=0 or Γ- point), compared to the acoustic branch below.

Additionally phonons are characterized through the direction of atomic displacement (phonon polarization) with respect to the phonon direction of propagation (phonon wavevektor). If the atoms that vibrate along the direction of phonon propagation, than the modes are longitudinal, whereas if the atoms vibrate perpendicular to the phonon propagation, these phonon modes are transversal. Altogether there are four different combinations of dispersion relation and phonon character: longitudinal optic (LO), transversal optic (TO), longitudinal acoustic (LA) and transversal acoustic (TA).

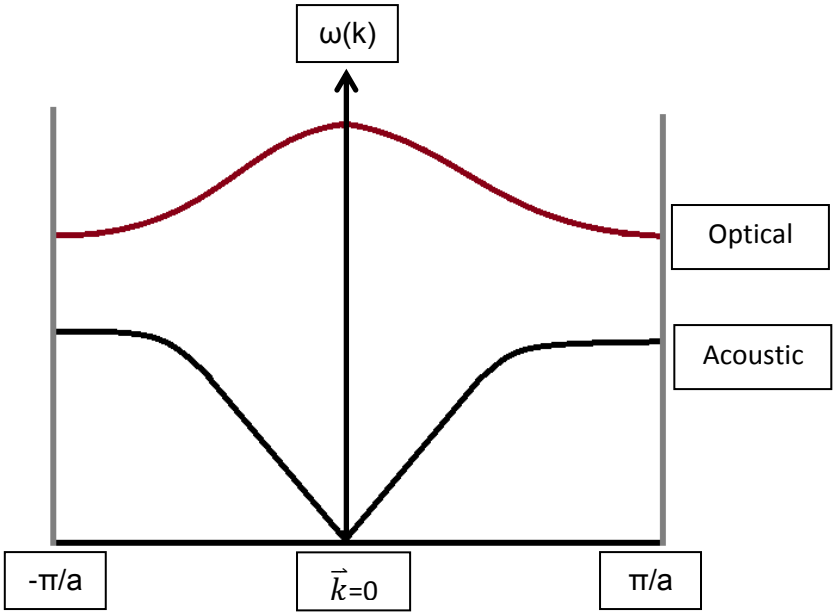

Fig. 7: Dispersion relation of a one-dimensional, diatomic chain. Optical phonons (red) have non-zero frequency for any wavevektor in the whole FBZ. Acoustic phonons (black), show strong dispersion and their frequency becomes zero at the FBZ center.

The atomic vibrations can be considered as a harmonic oscillators. The ratio between the interatomic force constants *K* and the reduced mass m determines the frequency ω of vibrations of bonded atoms:

$$\omega = \sqrt{\frac{k}{m}}$$

Raman scattering can be considered as a sequence of photon absorption and photon emission, as the incident (absorbed) and scattered (emitted) photon have different energies and wave vectors due to the difference in energies in interaction with phonons.

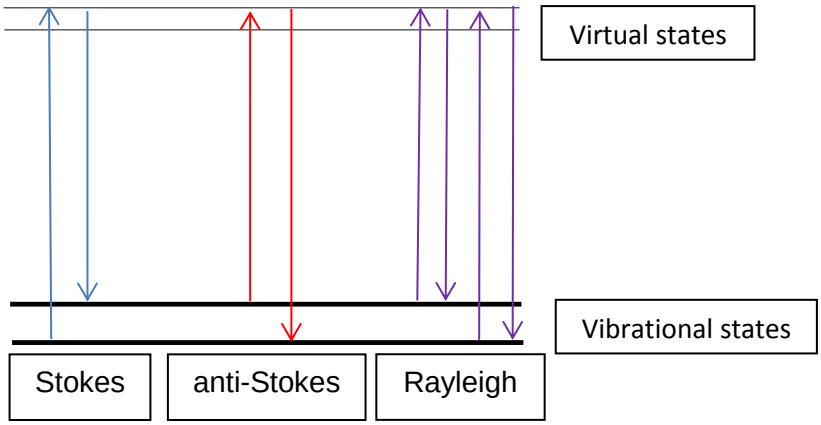

Fig. 8: Scattering effects. Stokes blue, anti-Stoke red and Rayleigh scattering violet.

Figure 8 schematically shows the two ways of photon scattering by phonons. The incident photon excites the sample to a virtual state and shortly after that it relaxes back to a vibrational state. In most cases the incident and the final vibrational state coincide and the photon keeps its incident energy. This elastically scattered photon produces the so called Rayleigh scattering. Since the probability for inelastic scattering is much smaller than for elastic scattering, only one of 10^6 to 10^8 photons are scattered inelastically [26]. Therefore the intensity of Raman inelastic scattering is considerably weaker compared to the intensity of the Rayleigh scattering. For the final vibrational state that has a higher energy than the incident level, the scattered photon shows a lower energy than the incident photon. This is called Stokes process. Anti-Stokes processes have an initial vibrational state with higher energy than the final state. For an anti-Stokes shift a higher vibrational level has already to be populated in order to increase the energy of a scattered photon.
The ratio between the intensity of Stokes and anti-Stokes inelastic scattering is given by

$$\frac{\mathrm{I\ anti-stokes}}{I\ stokes} = \frac{\tilde{\nu}s + \tilde{\nu}i}{\tilde{\nu}i - \tilde{\nu}s} e^{\frac{-\tilde{\nu}s}{K_B \cdot T}}$$

$\tilde{\nu}i$: is the wavenumber of the incident photo.
$\tilde{\nu}s$: is the wavenumber of the scattered photon.
K_B: is the Boltzmann constant.
T: is the absolute temperature.

The second term of the equation describes temperatures in which crystals can be studied without melting them, intensities of anti-Stokes are usually much weaker than the intensities

of Stokes. Nevertheless, the ratio between anti-Stokes and Stokes scattering increases with increasing temperature.

Not all phonons in the FBZ can be observed for Raman scattering. The scattering of a photon by a phonon must fit to the energy and momentum conservation law. This implies that only phonons with a wavevektor $\vec{k} \approx 0$, at the center of the FBZ at the Γ-point, can be observed. Phonons can be Raman-active, IR-active or silent. To be Raman-active the atom movement of a vibrational mode must induce a change of the polarizability.

$$P = \alpha \cdot E$$

P: is the polarization induced by an electric field E.
α: is the polarisability tensor.

Raman spectroscopy offers advantages in structural analysis. The temporal resolution is small-scaled due to the short lifetime of exited virtual states and Raman-process corresponds to the period of atomic vibrations and Raman scattering occurs within the range of a few unit cells.

The group theory and symmetry analysis proves the number of normal modes and their symmetry. The total irreducible representation of the Γ-point of zircon can be given from this as

$\Gamma = 2A_{1g}+A_{2g}+4B_{1g}+B_{2g}+5E_g+A_{1u}+2A_{2u}+B_{1u}+2B_u+4E_u$ [27, 28]

The A_{1g}, B_{1g}, B_{2g} and E_g modes are the 12 Raman active modes. The A_{2u} and E_u modes are active in the infrared. The general lattice dynamics properties of zircon are discussed well in both reports [27, 28].

WP	*A_{1g}*	*B_{1g}*	*B_{2g}*	*E_g*
16h	2	2	1	3
4b	0	1	0	1
4a	*0*	*1*	*0*	*1*

A_{1g}:			*B_{1g}*			*B_{2g}*			*E_g*			*E_g*		
a			c				d							-e
	a			-c		d					e			
		b								e		-e		

	A_{1g}	B_{1g}	B_{2g}	E_g	A_u	E_u
Zr		215		202	338	287
$Translation\ (SiO_4)$		393		225		
$Resticted\ rotations\ (SiO_4)$				356		389
$\nu\ 1\ ,(SiO_4)_{str}$	974				989	
$\nu\ 2\ ,(SiO_4)_{bend}$	439		266		608	
$\nu\ 3\ ,(SiO_4)_{str}$		1008		923		885
$\nu\ 4\ ,(SiO_4)_{bend}$		641		546		430

Table 2: Symmetry analysis of ZrSiO4. It shows the wave number and assignment of the observed Raman and IR modes [27, 28]

Raman spectroscopic measurements were performed at room temperature with a Horiba Jobin-Yvon T6400 triple monochromator system equipped with a liquid N_2-cooled CCD detector and an Olympus BH2 microscope. The spectra were collected in back-scattering geometry with a spectral resolution of 2 cm^{-1}. The diameter of the laser spot on the sample surface was approximately 1.5 µm. The power of the laser beam varied between 7.0 and 0.2 mW on the sample surface, to assure non-destructive experimental conditions. A laser line with 514.5 nm was used for the incident radiation. The zircon crystals were oriented with the c-axis perpendicular to the polarisation of the laser beam. The specimen was not well shaped, thus the orientation of the crystal axes could be derived by considering the scattering of the total irreducible representation (A_{1g}) .The wavenumber of the corresponding Raman peak is around 1008 cm^{-1}. With parallel polarized orientation this peak shows maximum intensity along [001], due to the fact that the Raman tensor possesses only diagonal non-vanishing elements. The experimental geometry remained unchanged as long as possible, after in/decreasing pressure. The Raman spectra were collected in the spectral range between 15 cm^{-1} and 1200 cm^{-1}. In addition to the spectra of the sample, the contribution of the diamond anvil cell has been measured. This includes the diamonds and the used pressure medium. To get clear sample spectra the spectra of the contribution has to be normalized to spectra of the sample and subtracted (Fig. 9).

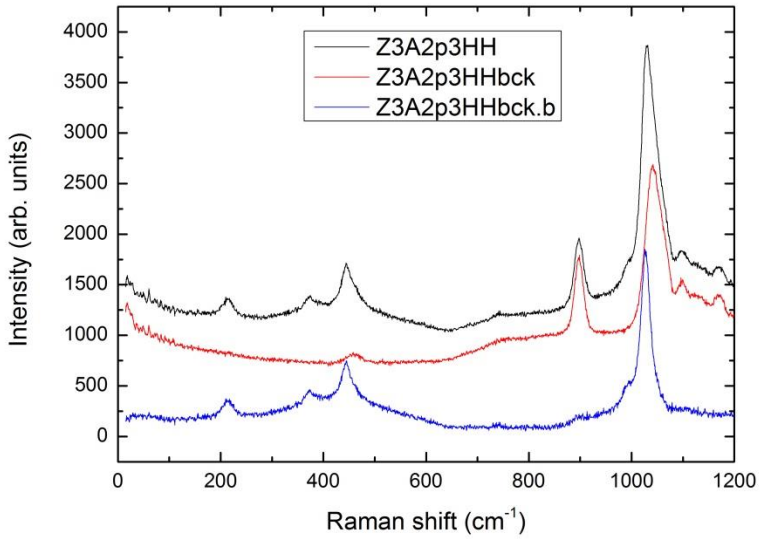

Fig. 9: Black spectrum shows the measured sample. Red spectrum is the normalized contribution spectrum and the blue spectrum is the result of the subtraction of both.

After this the Bose-Einstein correction was used on the resulting spectra. Finally the Raman spectra were corrected for the continuous luminescence-induced background by subtracting a fith-degree polynomial function (Fig. 10).

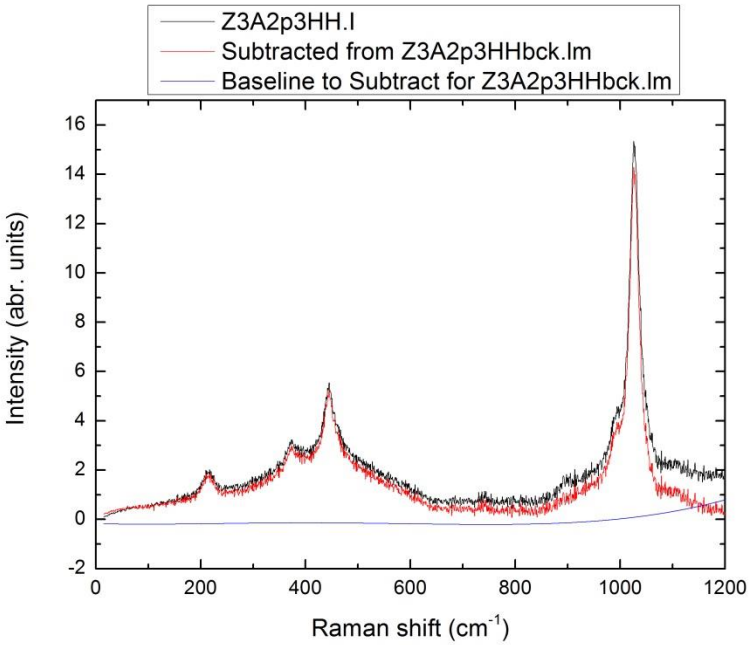

Fig. 10: Black Raman spectrum is before subtracting a five-degree polynomial function and the red spectrum is the final spectrum of the sample.

2.5 The Diamond-anvil-cell method

Material studies under high pressure conditions are possible using the combination of the diamond-anvil-cell (DAC) technique and the ruby luminescence method. Small culet areas induce high pressure in the inner part of a pressure chamber, by applying minimal external force (see Fig. 11). The primary components are:

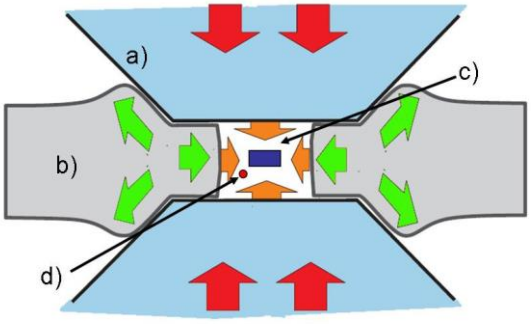

Fig. 11: Inside a diamond anvil cell. Showing the destribution of pressure and principal components of the DAC [29].

a. Diamond anvils
b. Gasket
c. Pressure medium
d. Pressure calibrant (Ruby)

The diamond anvil cell makes it possible to transfer uniaxial stress into hydrostatic pressure onto a sample. It relies on two opposed anvils for generating pressure. The diamond anvils are isolated by a gasket from getting into direct contact during the experiment. The gasket embeds the sample chamber. It is a hole in the middle of the gasket which contains the pressure transmitting medium, the pressure calibrant and the sample.

The pressure calibrant indicates the actual pressure inside the pressure chamber. There are two reasons why diamonds are used in DACs.

1. Diamond is the hardest existing material.
2. Diamonds is transparent for electromagnetic radiation in the infra-red, visible and ultra violet light and X-rays above 10keV.

For high pressure experiments, diamond with a brilliant cut has an enlarged culet surface. This cut generates stress on its girdle area, creating instability at a pressure above 50 GPa. The Boehler–Almax diamond cut (Fig. 14) is preferred for technical use in the DAC based on different table-girdle-pavilion ratios. Beveled culets surfaces were used for experiments in

100 GPa regions to withstand the pressure. The culet experiences additional sideways faces [29]. Figure 12 shows the change in the Raman scattering of diamonds due to the deformation of the diamond anvils during the experiment. The splitting of the F_{1g} Raman active mode of diamonds observed above 2 GPa is due to the so called morphic effect: lowering of the symmetry of the structure upon the application of external vector field. This leads to changes in the optical properties of the diamond and can influence the results.

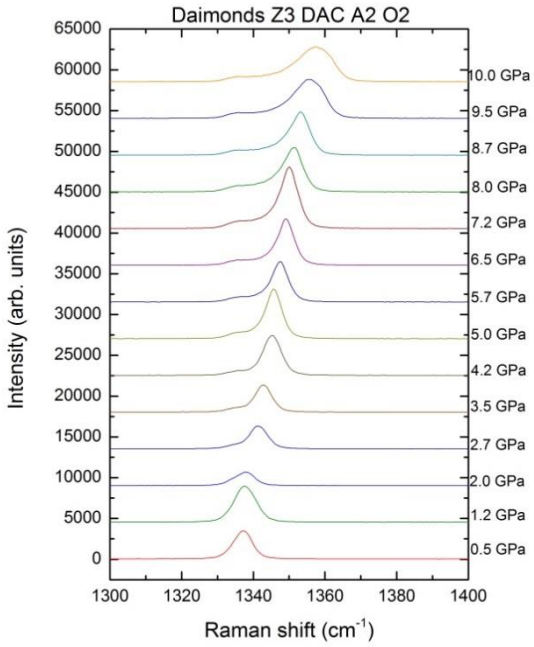

Fig. 12: Morphic of the diamond peak. Around 5 GPa the diamond peak starts to broaden and a weak second peak start to appear on its left side, due of the reduction of symmetry.

The elastic properties of the gasket secure the stability of the culets during the pressure loading and the experiment. The most commonly used gasket materials are stainless steel, Inconel Ni-Cr-Fe alloy, tungsten and rhenium. The gasket is a metal disc with a thickness between 250 µm and 300 µm. The gasket is pre-indented to avoid plastic deformation during the experiment. The compression of the gasket should not pass 70% of the initial thickness. After indentation a hole is drilled in the middle of the indented area. This can be made by spark eroding or laser ablation. Each technique varies in quality and cost. Mechanical drilling is fast and cheap but the result is of bad quality. Spark eroding costs more but produces a clean hole with nearly no micro cracks. Laser ablation is very expensive and ensures even better quality of gasket holes than spark eroding. A good gasket hole improves stability and lowers the risk of failures during the experiment, like crushing the sample or even the diamonds at high pressure or losing the sample or pressure medium during loading the cell.

The size of the hole depends on the culet size and the desired pressure to be achieved in the experiment. Advantage of stainless steel is that it is cheap and easy to drill. The size of the sample depends on the pressure of the experiment. High pressure leads to a smaller volume of the sample. However for high pressure experiments above 10 GPa as well as for high temperature/high pressure experiments rhenium gaskets are preferred. The sample thickness should be around 60% of the gasket thickness. DACs generating force by screws are relatively small and light. The screws have to be tightened in an appropriate sequence or by a gear tool. A benefit of the Boehler-Almax DAC is the carbide seats on which the diamonds recline. It makes it appropriate for synchrotron radiation. Another advantage is the improved anvil cut, reducing the attenuation of X-rays. [29]

A pressure medium is used to ensure the homogeneous distribution of stress in the gasket embedded pressure chamber. There exist several different pressure media in solid, liquid or gas form. One very important property of these is that they do not react with the sample during the experiment. Examples for pressure medium are alkali-halides (solid), neon (gas), methanol-ethanol mixture or methanol-ethanol-eater mixture (liquid). Methanol-ethanol, in the ratio 4:1, is a pressure transmitting medium with a hydrostatic pressure up to 9.8 GPa. Methanol-ethanol- water in ratio 16:4:1 has an extent hydrostatic pressure up to 10.5 GPa [30].

The ruby luminescence method is used for the pressure measurement in the diamond anvil cell and depends on the size, shape and the degree of crystallinity of the ruby. The most commonly used micro-crystal chips have considerable internal elastic strain. Ruby is a variety of corundum (α-Al2O3, $R\bar{3}c$), with Cr^{3+} partially substitution for Al. It contains 3000 to 5000 ppm of Cr^{3+}. Ruby does not undergo a phase transition for pressures under 100 GPa at room temperature. Cr^{3+} creates larger bonds with oxygen compared with Al leading to small elastic strain within the structure and an off-center displacement from the octahedral central positions. Due to the laser a strong fluorescence leads to a peak with double maxima. The electron state changes from the ground state $^4A_2$ to the metastases ^2E of Cr^{3+} in the distorted octahedral coordination [31, 32, 33, 34] (Fig. 13).

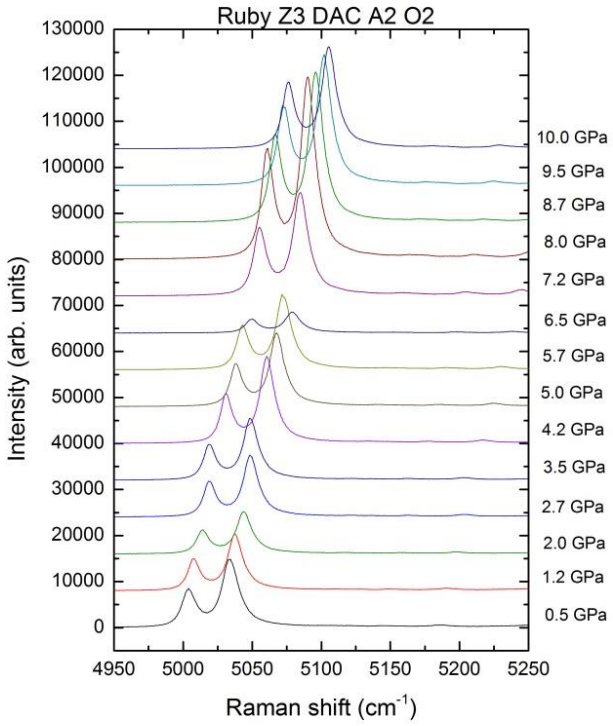

Fig.13: Ruby measured in DAC A2 with Raman spectroscopy with Raman shifts due to induced pressure.

The double maxima shift linearly with pressure. From the wavelength of the higher intensity peak, pressure can be calculated, according to the recalibrated ruby pressure scale: [35]

$$P = \frac{A}{B} \cdot \left(\left(1 + \left(\frac{\Delta\lambda}{\lambda 0} \right) \right)^{B} - 1 \right) \text{[35]}$$

P: Pressure (Mbar)

A: 19.04 Mbar

B: Initial slope 7.59 by hydrostatic condition

$\Delta\lambda$: Wavelength of measured ruby

$\lambda_{0:}$ Calibration wavelength 5029 cm^{-1}

B is 7.59 ± 0.04 cm^{-1}/GPa, an empirically determined coefficient for hydrostatic conditions [36]. The disadvantage of this calibration method is its sensivity to temperature [37, 38]. Compounds contaminated with rare earth elements have exhibited luminescent features similar to ruby, but with marginal temperature dependence. For example Sm^{2+} doped

compounds show no sensitivity to temperature variation and up to a 4 time's larger wavelength shift [29, 39].

Daimond Almax cells technical informations:

Cell	Culet diameter (µm)	Bevel	Bevel diameter (µm)	Total diameter (mm)	Angel between culet face and diamond faces	Opening angle	Total height (mm)	Bottom height (mm)	Bottom diameter (mm)
A1	500	none	none	4,0	25°	80°	1.95	0.7	3.19
A2	600	none	none	4,0	25°	80°	1.95	0.7	3.19
A3	600	Single, 8°	700	3,3	15°	85°	1.43	0.692	2.5

All three Almax cells have in common:

Rim height (mm)	Conical angle	Number of diamond faces
0.3	60°	16

Figure 14: Technical drawing of the diamond for the DAC.

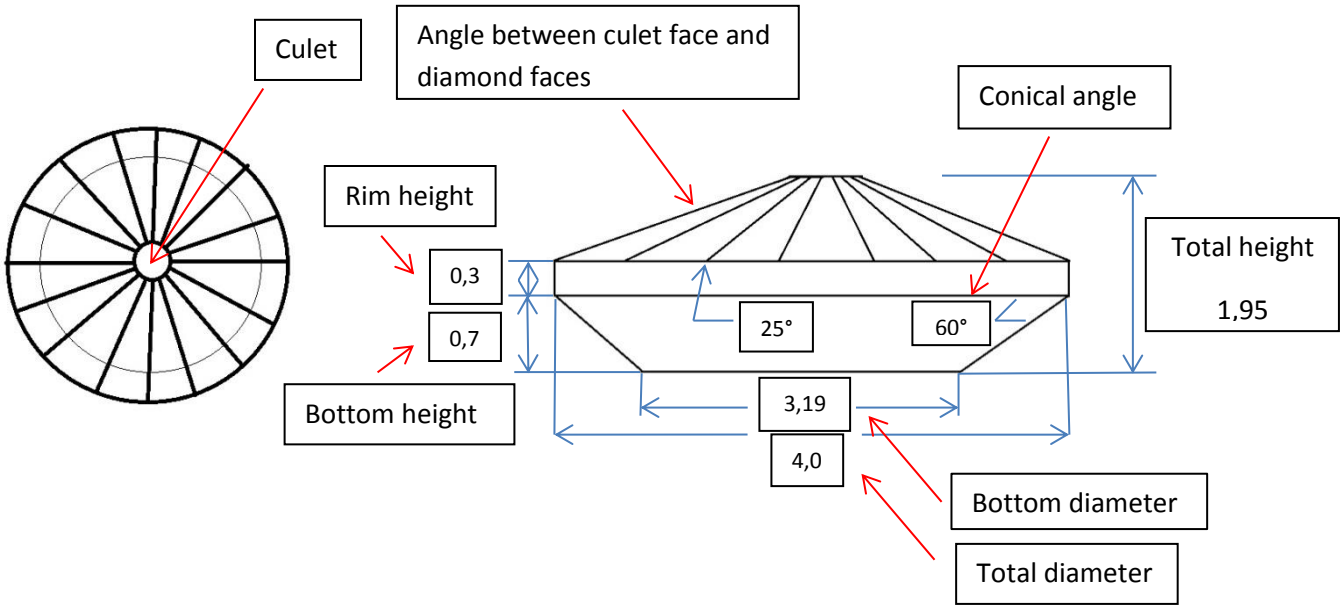

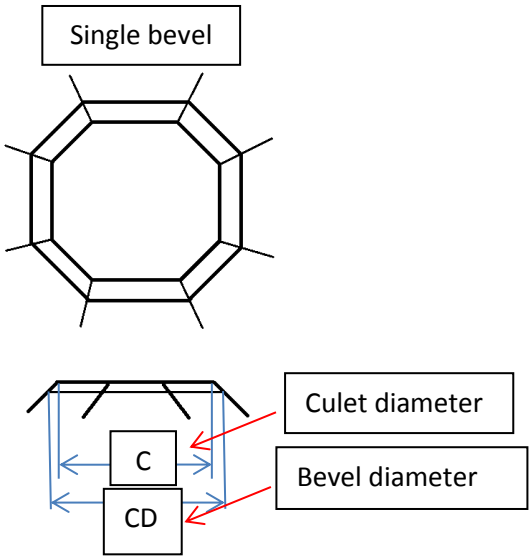

Pressure Medium for these experiments:

Medium	Hydrostatic pressure limit (GPa)
Methanol : Ethanol = 4:1	9.8
Methanol : Ethanol : Water = 16:3:1	10.5

3. Results

3.1 XRD

X-ray diffraction was used to determine the crystallite sizes of the weakly metamict zircon and the intermediate metamict zircon. With the Scherrer equation it is possible to calculate the crystallites size knowing the wavelength λ, the angel θ and the full width at half maximum (FWHM) of a Peak**.**

$$L = \frac{k \cdot \lambda}{\Gamma \cdot cos\ \theta}$$

L: Size of crystallites.

k: is a dimensionless shape factor here 1.

λ: X-ray wavelength 1. 5418 Å was used (overlapping α1 and α2 wavelength).

Γ: FWHM of Bragg reflections in radians.

θ: diffraction angle in radians.

The technique is however limited in the range of nano size particles.

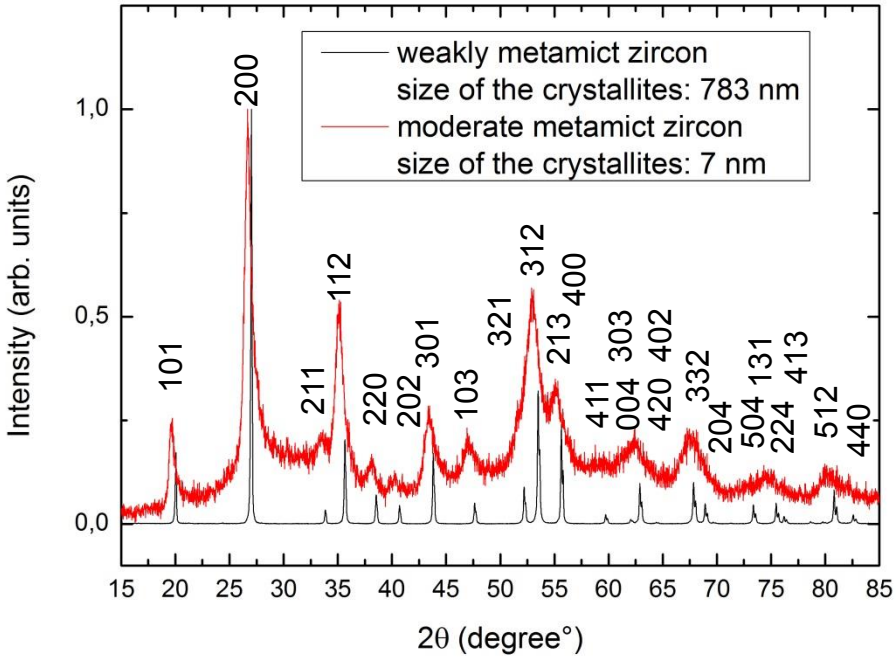

Fig.15: X-ray powder diffraction pattern of weakly- and moderate metamict zircon. The moderate metamict zircon is red and the weakly metamict zircon is black. The moderate metamict zircon shows compared to the weakly metamict zircon broadened peaks, shift in the peaks position, loss in intensity and well pronounced amorphous peaks beneath the crystalline ones.

Figure 15 shows the result of the X-ray diffraction measurement. The weakly and intermediate metamict zircon can be well distinguished. The weakly metamict zircon shows well defined Bragg peaks with clear shoulders of the α_2 radiation, increasing with larger 2θ values. It shows a well crystalline pattern. The moderately metamict zircon shows a significant degree of structural disorder. The long range order is disturbed and an increase of the FWHM of the Bragg peaks can be seen as the result. The intensity is normalized for better comparison, but there occurs a huge loss of intensity in the moderate metamict zircon. The Bragg peak at 27°, respectively 24° in both metamict zircons has the highest intensity. This Bragg peak was used for the particle size determination with an FWHM of weakly metamict zircon of 0.116° and for the intermediate zircon of 0.723°. Using the Scherrer equation and the position and the FWHM of the most intense Bragg peak, allows to determine the size of the crystallites for weakly metamict zircon of 783 nm and for the intermediate metamict zircon 7 nm. The latter is an approximation, because the Scherrer equation holds best for particle sizes <100 nm and >10 nm. The patterns require refinements for more exact results, in their current state they leave room for possibly large errors.

3.2 EMPA

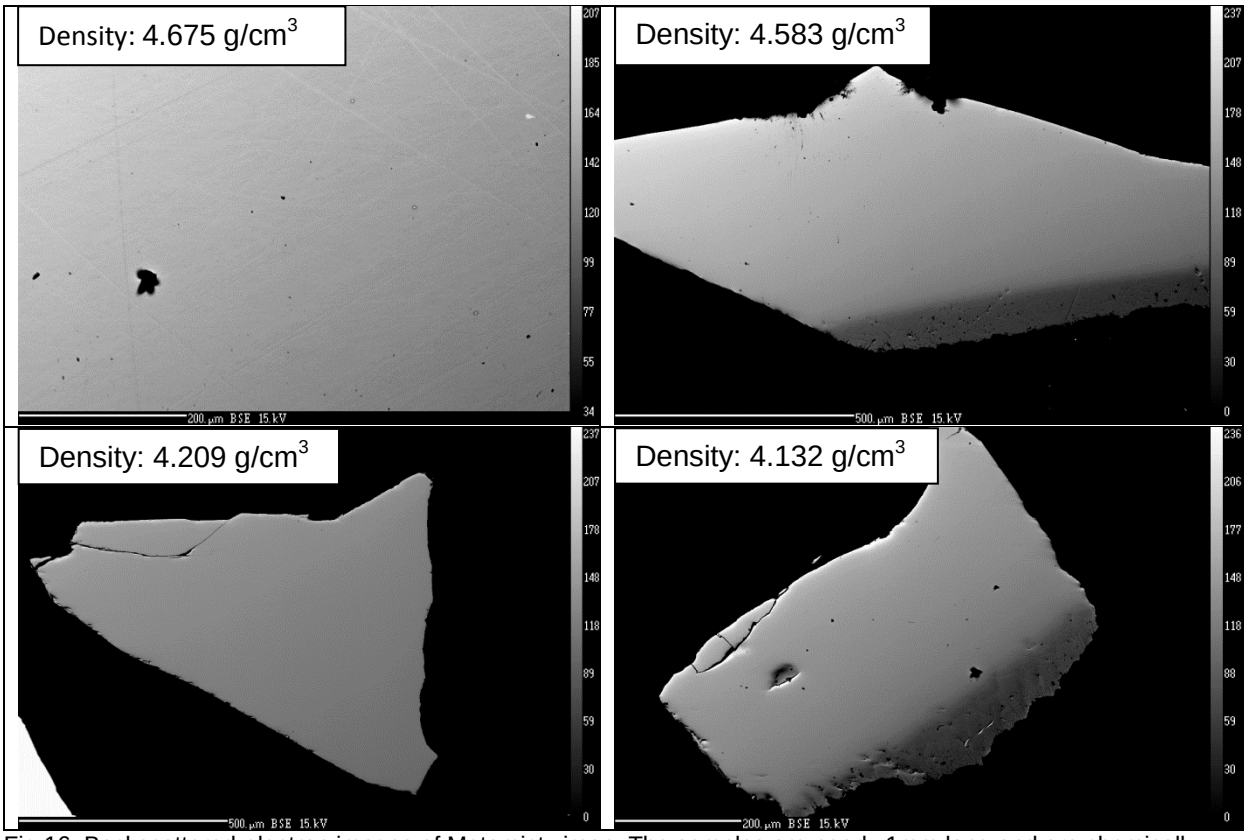

Fig.16: Backscattered-electron images of Metamict zircon. The samples are nearly 1mm long and are chemically homogenous.

The backscattered-electron images of all samples organized by their densities (Fig. 16). The samples are nearly 1mm long and appear to be chemically homogenous.

Sample	SiO_2	P_2O_5	Y_2O_3	ZrO_2	HfO_2	U_2O_3	Total
Z7	31.91	0.04	-	67.72	0.72	-	100.38
Z1	32.48	0.04	-	66.31	1.32	0.16	100.17
Z3	31.40	0.02	0.07	66.40	1.58	0.38	99.90
Z4	31.68	-	-	66.44	1.61	0.37	99.81

Table 3: The here shown results are the median of the EMPA measurement of all detected chemical elements.

The chemical compositions of Z7, Z1 and Z4 were determined by averaging over 30 spatial points, whereas for Z1 the averaging was performed over 21 points. Table 3 shows all the oxides that could be detected. The content of Al_2O_3, CaO, MnO, FeO, La_2O_3, Ce_2O_3, Nd_2O_3, Gd_2O_3, PbO and ThO_2 were lower than the detection limit. The total medians show the quality of the measurement. All presented results are within the tolerated margin of error. Analyses are given in terms of oxides of the elements. Calculating the mineral formula gave the following results:

Z7: $Zr_{1.034}\,Hf_{0.006}\,Si_{0.998}\,P_{0.001}\,O_4$

Z1: $Zr_{0.993}\,Hf_{0.012}\,U_{0.001}\,Si_{0.999}\,P_{0.001}\,O_4$

Z3: $Zr_{1.030}\,Hf_{0.014}\,U_{0.003}\,Y_{0.001}\,Si_{0.999}\,P_{0.001}\,O_4$

Z4: $Zr_{1.023}\,Hf_{0.015}\,U_{0.003}\,Si_{0.999}\,O_4$

The results show that all zircons have different chemical compositions. In all four samples the fractions of Zirconium and Silicon are more or less unchanged. The content of Hafnium and Uranium increases with the decrease of density. This can be considered for the origin of the different degree of metamictization, keeping in mind that Z1, Z3 and Z4 have all the same age.

$$D_\alpha = 8 \cdot \frac{c_U \cdot N_A \cdot 0.9928}{M_{238} \cdot 10^6} \cdot \left(e^{\lambda_{238} t} - 1\right) + 7 \cdot \frac{c_U \cdot N_A \cdot 0.0072}{M_{235} \cdot 10^6} \cdot \left(e^{\lambda_{235} t} - 1\right) + 6 \cdot \frac{c_{Th} \cdot N_A}{M_{232} \cdot 10^6} \cdot \left(e^{\lambda_{232} t} - 1\right)$$

Fig.17: Formula to calculate the dose of metamict zircon [40].

The dose was calculated via the formula given by Nasdala [40] (Fig. 17). It follows a list of all values, which are used to calculate the dose for each sample.

Measured actinides concentration

Samples	U (ppm)	Th (ppm)
Z7	100±200	130±150
Z1	1400±100	160±130
Z3	3000±1000	350±170
Z4	3400±100	340±60

Table 4: Measured Uranium and Thorium in all samples in parts per million (ppm)

Avogadro´s number

N_A: $6.02214 \cdot 10^{23}$ mol^{-1}

Molecular weight of parent isotopes [40, 41, 42]:

M_{238}: 238.05078 g/mol

M_{235}: 235.04392 g/mol

M_{232}: 232.03805 g/mol

Respective decay contents [43]:

λ_{238}: 1.55125· 10^{10} years

λ_{235}: 9.8485· 10^{10} years

λ_{232}: 0.49475· 10^{10} years

t: age of zircon.

0.9928 for U_{238}, 0.0072 for U_{235} and 1 for Th_{232} represent the isotopic composition as constants. In the opinion of the Subcommittee for Isotopic Abundance Measurements (SIAM), these values represent the isotopic composition of the chemicals, most commonly encountered in the laboratory [44, 45].
The low concentration of U and Th in Z7, leads to high errors for the measurement and the result. This proofs that Z7 is really weak metamict. The assumption that the density can describe the degree of metamictization can be confirmed with table 5. Higher dose leads to a decrease of density. Z3 and Z4 have within the margin of error nearly the same dose and density.

Sample	Density	Dose	±Dose
	(g/cm^3)	decay\g(event/g)*10^{18}	decay\g(event/g)*10^{18}
Z7	4.675	0.1	0.2
Z1	4.583	2.9	0.3
Z3	4.209	6.8	0.3
Z4	4.132	5.8	0.3

Table 5: Comparing the samples in relation of their density and dose. It can be confirmed that Dose influence the density of the sample.

3.3 Raman spectroscopy

Nine specimens were measured by Raman spectroscopy. Three from Z7, three from Z1, two from Z3 and one from Z4. This was done to show the reproducibility of the resulting spectra. The most samples were measured twice and an additional time to combine Raman spectroscopy with single crystal synchrotron X-ray diffraction, to learn about the influence of crystallite rearrangement on the structure. The synchrotron analysis of XRD will not be discussed in this study. The size of the specimen loaded in the diamond anvil cell was approximately 50 µm x 50 µm x 50 µm. The pressure media used in this study were methanol:ethanol in a ratio of 4:1 or methnaol:ethanol:water in ratio 16:3:1, to ensure a hydrostatic pressure up to ~10 GPa.

All samples were measured in parallel polarization scattering geometry with the crystallographic c-axis parallel or perpendicular to E_i (thus the polarization of radiant light E_i ‖ to the polarization of scattered light E_s). Sample Z1 and Z3 were additionally measured in

cross polarized scattering geometry ($E_i \perp E_s$). Here we only discuss the parallel polarized spectra measured with the c-axis perpendicular to E_i ($\bar{Y}(XX)Y$ geometry in Porto´s notation, where X and Y correspond with the crystallographic a- and b- axis of zircon). The scattering geometry was verified to represent the best of both, the crystalline and amorphous Raman signal.

The Raman spectra, with a polarization $\bar{Y}(XX)Y$ at ambient pressure, can be distinguished well (Fig. 18). The weakly metamict zircon Z7 show well resolved sharp peaks (Fig. 18). By increasing the dose the peak position decreases (compare Z7->Z1->Z3, Z4), the FWHM broaden and an amorphous peak appears beneath the crystalline one. The Raman peak at 356 cm^{-1} seems to disappear and the three peaks near 200 cm^{-1} (Fig. 18) merge into one broad peak. When the degree of metamictization increase for a small radiation dose the small peak at 393 cm^{-1} disappear.

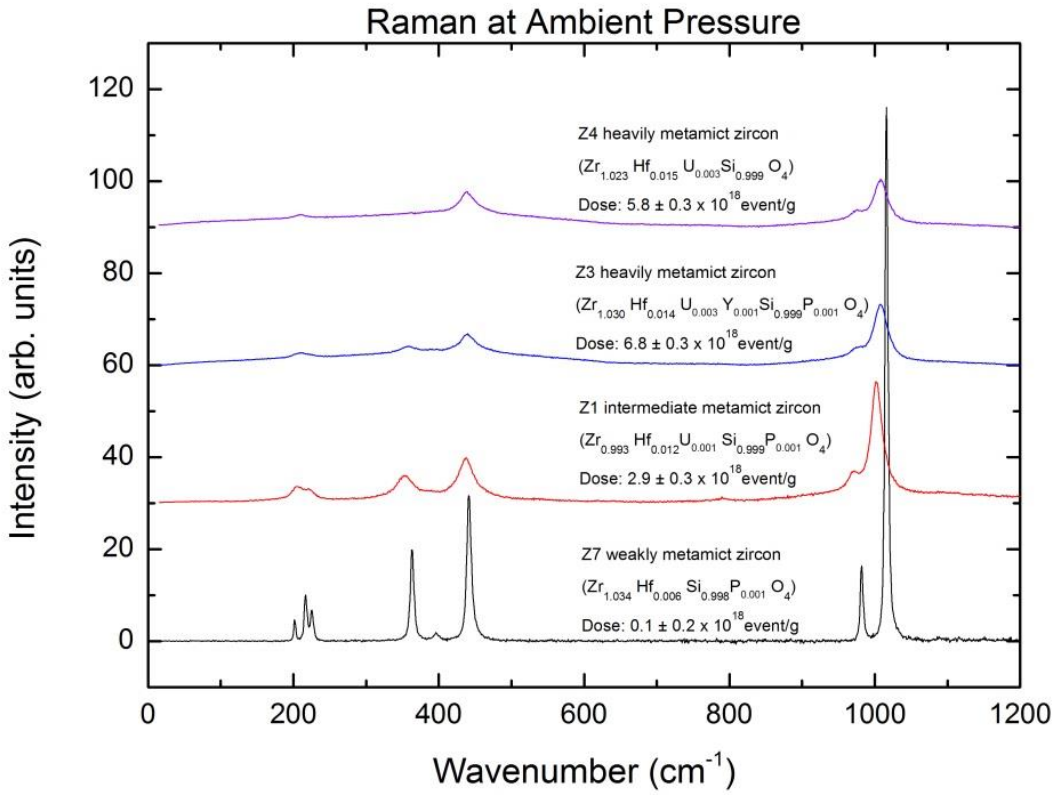

Fig.18: Raman spectra of all representativ samples ordered by their degree of metamictization at ambient pressure. Including information of their chemical composition and dose.

This study was focused on the pressure evolution of the four crystalline peaks at 1008 cm^{-1}, 976 cm^{-1}, 440 cm^{-1} and 356 cm^{-1} and the two amorphous peaks near 439 cm^{-1} and 996 cm^{-1} (Fig. 19). The strongest peak at 1008 cm^{-1} is generated by the B_{1g} mode due to the anti-symmetrical stretching of the SiO_4 tetrahedra. The peak at 976 cm^{-1} corresponds to the A_{1g}

mode resulting from symmetrical stretching of the SiO_4 therahedra. The peak near 440 cm^{-1} arises from A_{1g} due to symmetrical SiO_4 bending. The peak near 356 cm^{-1} results from E_g mode and it has been assigned to the anti-symmetrical SiO_4 bending [28] or SiO_4 rotational mode [27].

The amorphous Raman peaks cannot be attributed to any irreducible representation. They do not originate from phonons (which can be expected in a periodic system) but from vibrational density of states. Nevertheless the positions of the amorphous peaks are indicative of the type of atomic vibration in term of stretching, bending, rotation and translation. Those vibrations are associated with single “blurred” peak of the corresponding crystalline peaks. The amorphous peak at

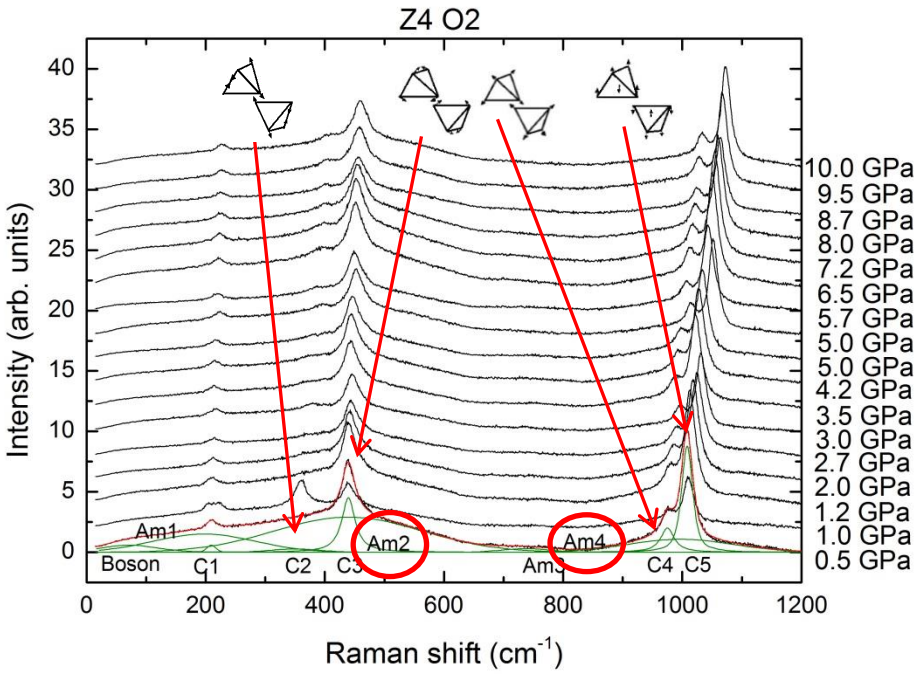

Fig. 19: Show the pressure evolution spectrum of the heavy metamict zircon Z4, with all fitted and relevant peaks of this study. It also can be seen Raman shifts due to pressure. The spectrum at 1 GPa is different due to the sample flip over inside the chamber while decompressing.

996 cm^{-1} is a mixture of the symmetrical and anti-symmetrical stretching of the SiO_4 tetrahedra. Its maximum is near of the peak at 1008 cm^{-1}. The amorphous peak near 439 cm^{-1} is most probably detmined by SiO_4 bending.

This thesis is emphazied on the change of the wavenumber and the FWHM. Normalized intensity of the amorphous fraction is plotted against pressure to see if there is some pressure dependence of the amorphous fraction. The weakly metamict zircon was measssured three times. Raman spectra were fitted in two different ways because the specimen meassured at DESY exhibit a weak amorphous peak at 266 cm^{-1}.

All samples show the same 8 peaks that were expected by group theory in this orientation (Fig. 20). All peaks are sharp and show changes to higher wavenumber with pressure with exception of C1 near 205 cm^{-1}. The crystalline peak has been attributed to Zr-SiO_4 translation. Most probably its softening with pressure is due to approches to the phase transition to a scheelite type structure, observed for pure crystalline $ZrSiO_4$ at 12.5 GPa [46].

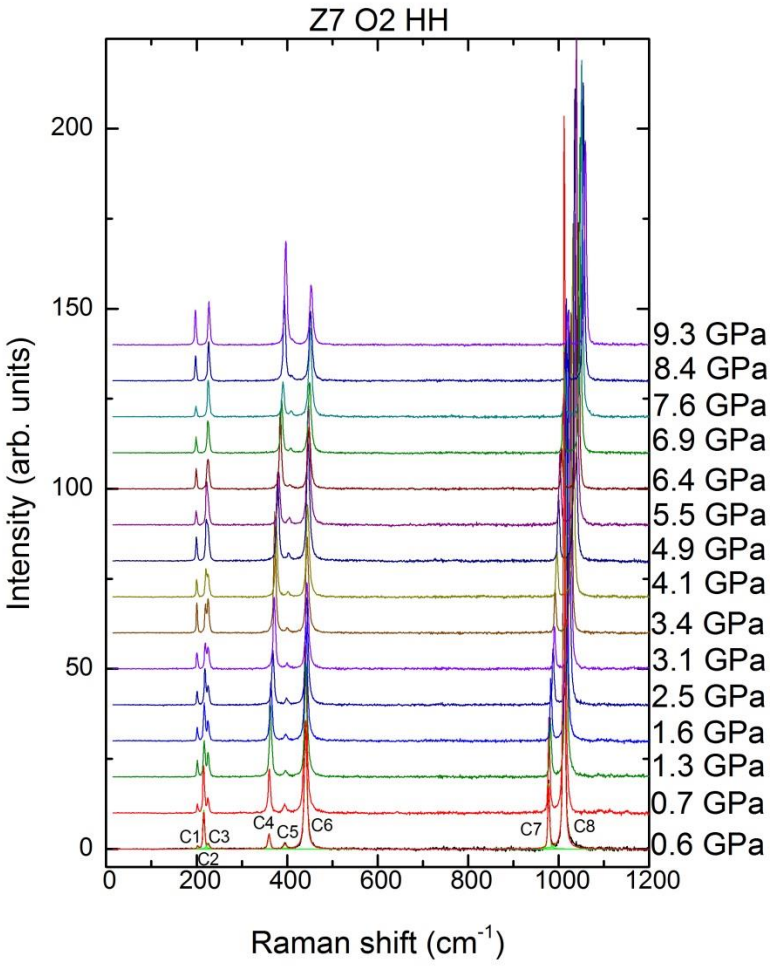

Fig. 20: Spectrum of the pressure evolution of the weaky meatmict zircon meassured parallel polarized.

The shift to higher wavenumber is due to the decrease in the samples volume of the sample by increased pressure. By increasing pressure the atomic bonds shorten. This leads to a higher force constant of the bonding. As just know of the theoretical Raman part the wavenumber can be expressed by:

$$\omega = \sqrt{\frac{k}{m}}$$

Since the mass remains the same, the pressure-induced increase in ω is due to the increase of the force constant (Fig. 21a). The FWHM in Raman spectroscopy depend on the local environments of the atoms involved in the vibration .Therefore crystals which do not undergo any structural change due to pressure the FWHM of the Raman peak should remain constant. All specimens from sample Z7 do not show any change in the FWHM, within uncertainties, with increasing pressure. Therefore sample Z7 behaves like a well crystalline zircon. For example, the pressure dependance of the crystalline peak C4 (C stand for crystalline peak) at 356 cm^{-1} and its FWHM for Z7 are shown in Figure 21b. All other Peaks show the same trend (see the appendix).

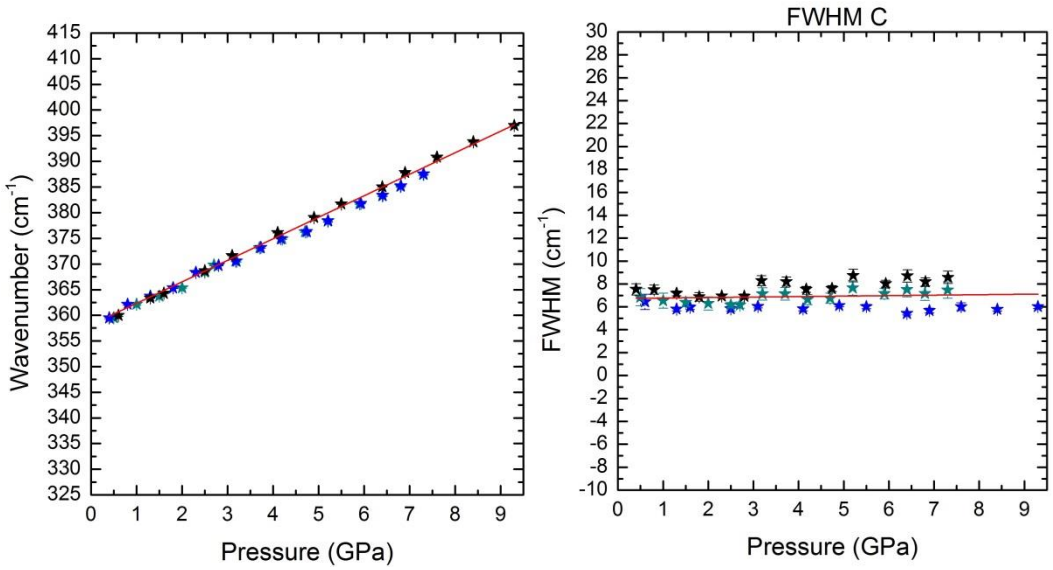

Fig. 21: **21a.** Peak C4 shows a linear Raman shift due to increased pressure for Z7. **21b.** shows the corresponding FWHM of C4. No changes can be detected as expected for well crystalline materials.

The moderate metamict zircon Z1 was measured three times. The Raman data sets from two of the specimen look very similar, whereas the spectrum of the specimen for the DESY measurement is structurally different regarding the relative intensities due to visible mismatches in the sample orientation (Fig. 22). The DESY sample has more pronounced metamict peaks and a higher intensity of the peak at 356 cm^{-1}. There are well pronounced metamict peaks. Their maxima are near the crystalline peaks at 440 cm^{-1} and 1008 cm^{-1} in each moderate and heavy metamict zircon sample. Another difference in comparison to the weakly metamict zircon is that in the moderate metamict zircon only 6 crystalline peaks can

be detected. For the two similar samples the peaks at 205 cm^{-1}, 215 cm^{-1} and 225 cm^{-1} cannot be distinguished. In the DESY sample the peaks at 215 cm^{-1} and 225 cm^{-1} ´look like one. The peak at 205 cm^{-1} is still well pronounced. The peak at 393 cm^{-1} disappears with the huge amorphous peak. Only for specimen of the sample measured at DESY could the boson peak be detected in sample Z1. The boson peak is generated by low energy excitation typical for amorphous solids. It is expected to be observed in zircon with high degree of metamictization and its intensity depends on the amount of amorphous fraction.

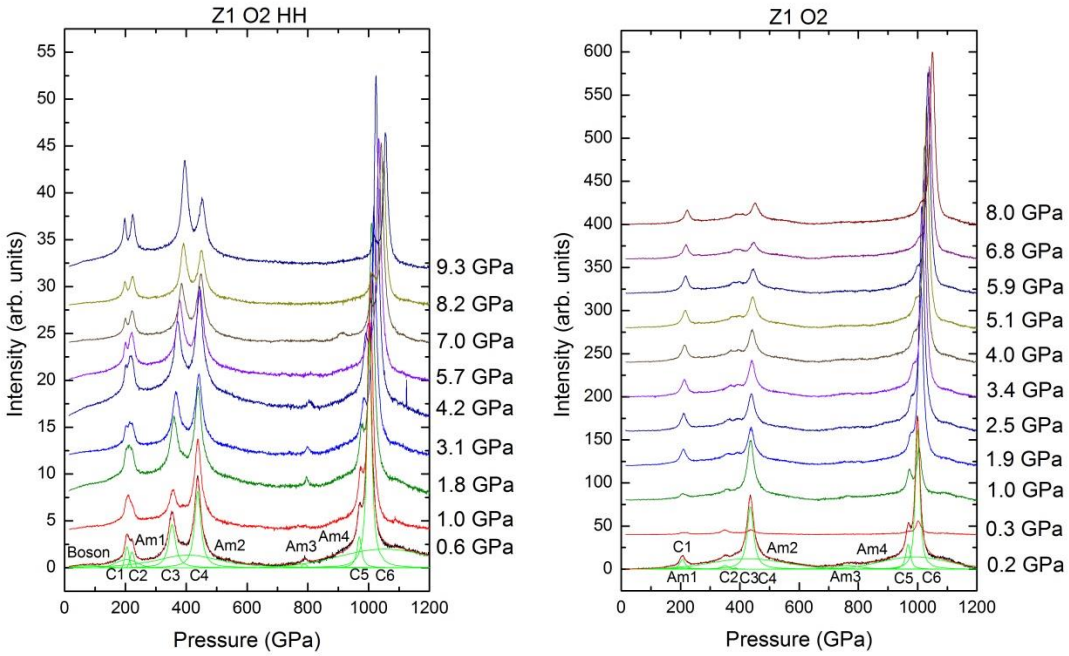

Fig. 22: On the left the moderate metamict zircon measured at DESY and on the right measured for this study.

Even if the crystal shows chemical homogeneity in the backscattered images, the Raman spectra show strong structural inhomogeneities. It will be shown that the three measurements do not show identical trends. . As shown in the above figure (Fig. 23) the specimen analysis of the moderate metamict zircons carried out in house (red and violet points) shows a different trend than the analysis carried out by DESY (blue points). The differences in this sample can also be seen in Fig. 23, 24 and 25. The amorphous peak at 439 cm^{-1} measured at DESY seems to follow a linear trend (Fig. 23a, green line). The other two specimens have an interruption around 2 GPa (Fig. 23a, indicated by a red arrow). The wavenumber of those decreases up to 2 GPa and start to increase after an interruption (Fig. 23a, red line). This decrease in wavenumbers can be explained through the softening of the zircon. The amorphous fraction can be considered as softer than the crystalline fraction due to the radiation-induced disorder. Breaking atomic bonds leads to an increase in the volume

of the crystal. Due to this the amorphous fractions can be easily compressed to a certain volume. Based on shortage of space it is more difficult to compress to these fractions and leads to behavior like the crystalline fraction, which can be seen by the increasing wavenumber in the spectrum.

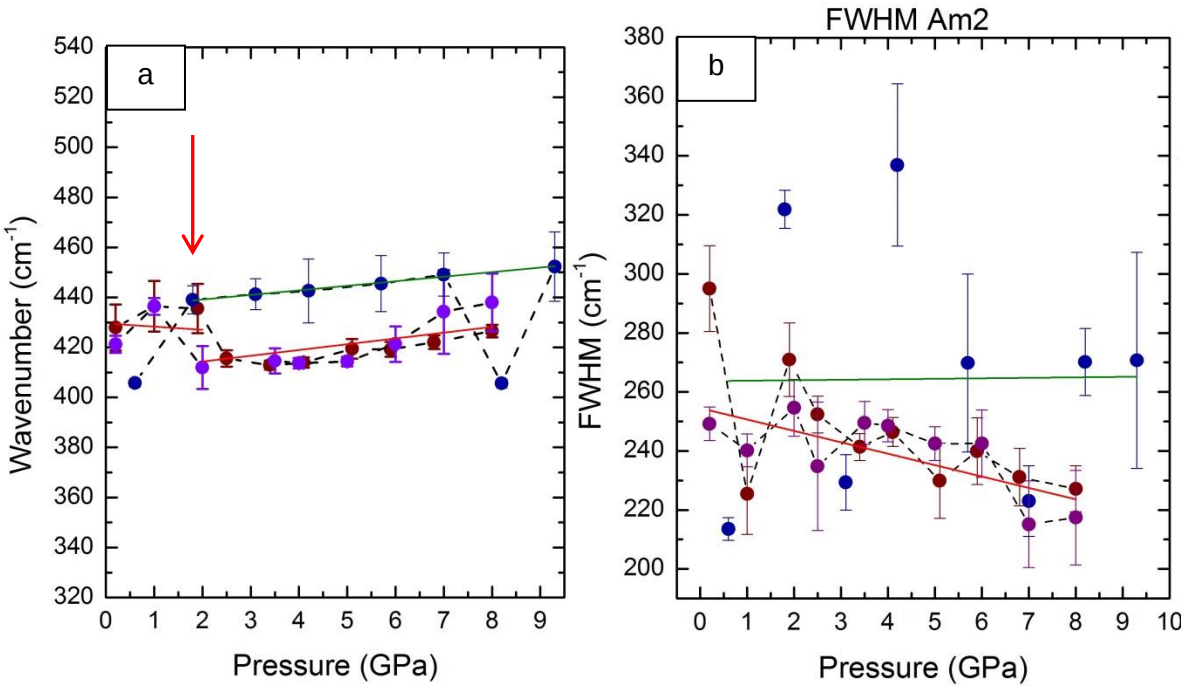

Fig. 23: Pressure dependencies of the wavenumber (a) and FWHM (b) of the SiO4 bending in the amorphous fraction in sample Z1. The violet and wine red points represent the specimens measured on only in house. The blue pinots represent the specimen measured at DESY. The red line represents the trends of all specimens or when there are anomalies the specimens measured in house. The green line represents the trend of the specimen measured at DESY. The arrow in (a) points to the anomaly in the wavenumber of the amorphous peak.

Another consequence of the volume reduction can be seen in the FWHM of the same peak. Atomic distances shorten and start to rearrange. This can change the coordination of some elements. This can be seen in Figure 23b. The specimen for the DESY measurements shows a linear trend of the FWHM (green line). The other specimen show a decrease of the FWHM which was just described (red line).

The crystalline peak at 356 cm^{-1} shows a normal crystalline trend. It does not show any reaction to the change of the amorphous peak (Fig.24a). But there is some change of the FWHM at 2 GPa for the two specimens measured in the University of Hamburg (Fig. 24b, see red arrow). A maximum can be seen for those with a minimum at 2.5 GPa. This can be due to the changes of the amorphous peak at 439 cm^{-1}. The FWHM of the specimen from the DESY measurements show a linear decrease within the uncertainties. This indicates that the crystalline peak also has to rearrange to accumulate the pressure. Both peaks seem to interact somehow.

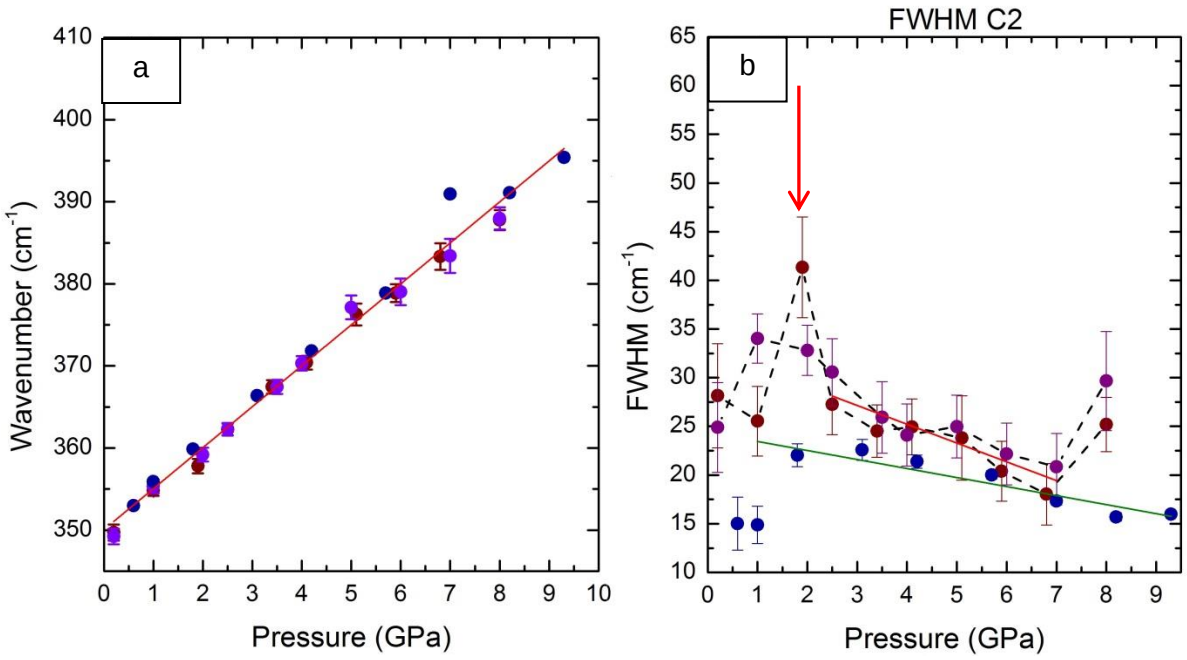

Fig. 24: Pressure dependencies of the wavenumber (a) and FWHM (b) of the symmetrical SiO_4 anti-symmetrical bending or SiO_4- rotation of the crystalline fraction in sample Z1. The violet and wine red points represent the specimens measured on only in house. The blue pinots represent the specimen measured at DESY. The red line represents the trends of all specimens or when there are anomalies the specimens measured in house. The green line represents the trend of the specimen measured at DESY. The arrow in (d) points to the anomaly in the FWHM of the crystalline peak.

The plot of the amorphous peak at 996 cm^{-1} has a minimum around 2 GPa (Fig.25a). Compared with the amorphous peak at 439 cm^{-1} there is no interruption like before. It is a gradual change. After 2 GPa the wavenumber increases. The FWHM decreases up to 5 GPA. After applying this pressure it remains more or less constant (Fig. 25b). The plot for the symmetrical stretching of the SiO_4 bond does not show any anomaly and increases with pressure as expected (Fig. 25c). The FWHM of the symmetrical stretching shows a minimum around 2 GPa. The FWHM decreases up to 2 GPa and increases after the minimum. This happens for the specimens measured especially for this study. The additional specimen shows no changes in the FWHM. The DESY measured sample does not change its FWHM. The other two have a minimum around 2 GPa (Fig. 25d).

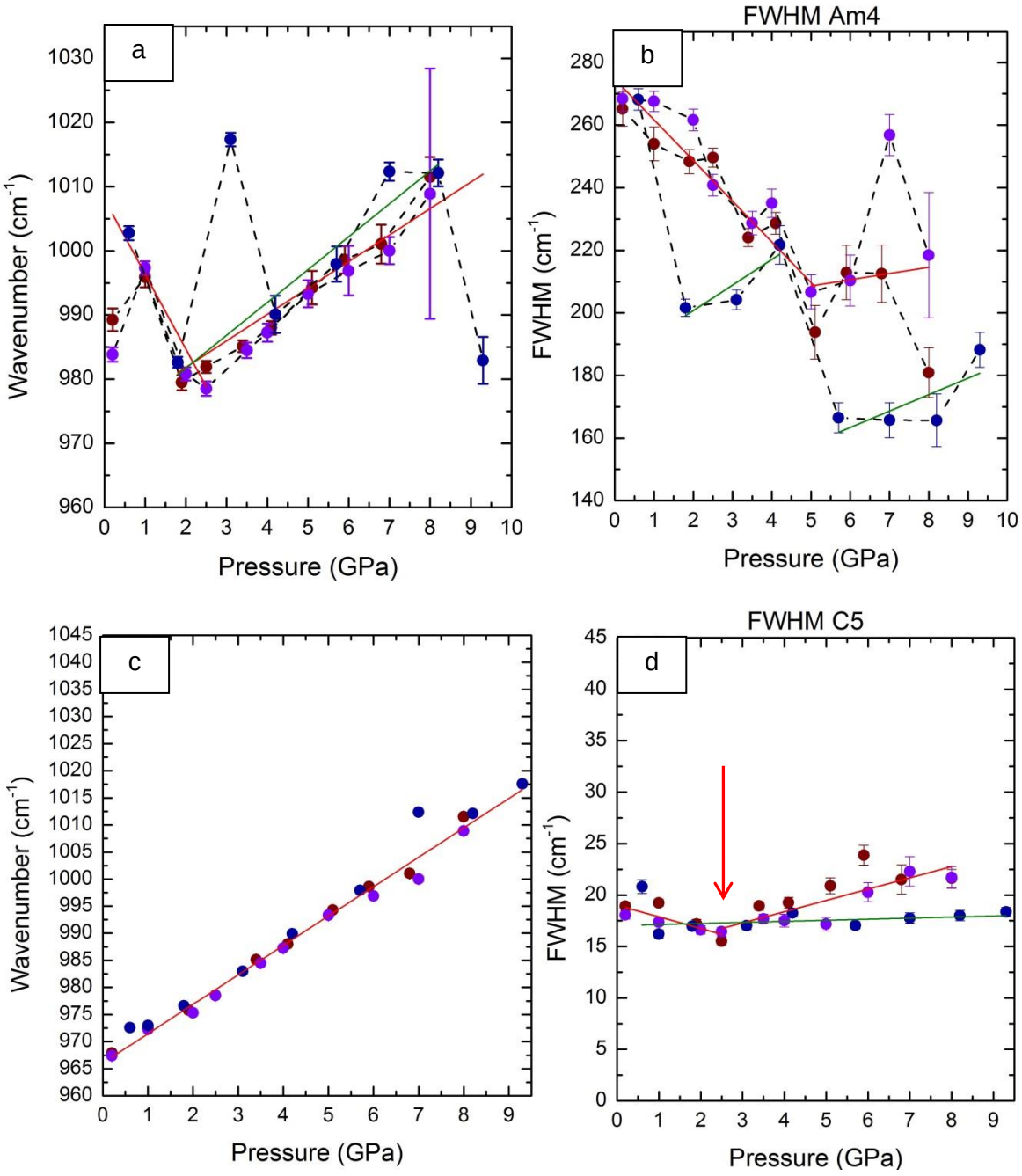

Fig. 26: Pressure dependencies of the wavenumber (a) and FWHM (b) of the SiO4 stretching in the amorphous fraction as well as pressure dependencies of the wavenumber (c) and FWHM (d) of the symmetrical SiO_4 stretching of the crystalline fraction in sample Z1. The violet and wine red points represent the specimens measured on only in house. The blue pinots represent the specimen measured at DESY. The red line represents the trends of all specimens or when there are anomalies the specimens measured in house. The green line represents the trend of the specimen measured at DESY. The arrow in (d) points to the anomaly in the FWHM of the crystalline peak.

In summary this trends indicate an interaction between amorphous and crystalline fraction. The stretching SiO_4 in both amorphous and crystalline nanoregions have an anomaly around 2 GPa. The structure tries to accumulate the pressure by rearranging the SiO_4 tetrahedra. However in some areas the structural alteration is predominantly in the amorphous regions

(e.g. the specimen of sample Z1 measured at DESY), while the crystalline nanoregions remain intact in this case.

Two specimens were measured from heavy metamict sample Z3. Both spectra look very similar and have a Boson peak, but with different intensities (Fig. 26). The specimen measured at DESY has a higher intensity than the other measured for this study. The specimen measured only in house shows a peak splitting starting at 4.2 GPa. This is due to the changes in the optical properties of the diamond anvils, leading to partial depolarization and enhancement of the E_g mode, which are in general not allowed in this scattering geometry. Additionally the peak near 202 cm^{-1} is known to have negative dω/dp, [47] while the neighboring peak of 225 cm^{-1} has a positive dω/dp, which enhances the wavenumber difference of these two peaks with increasing pressure.

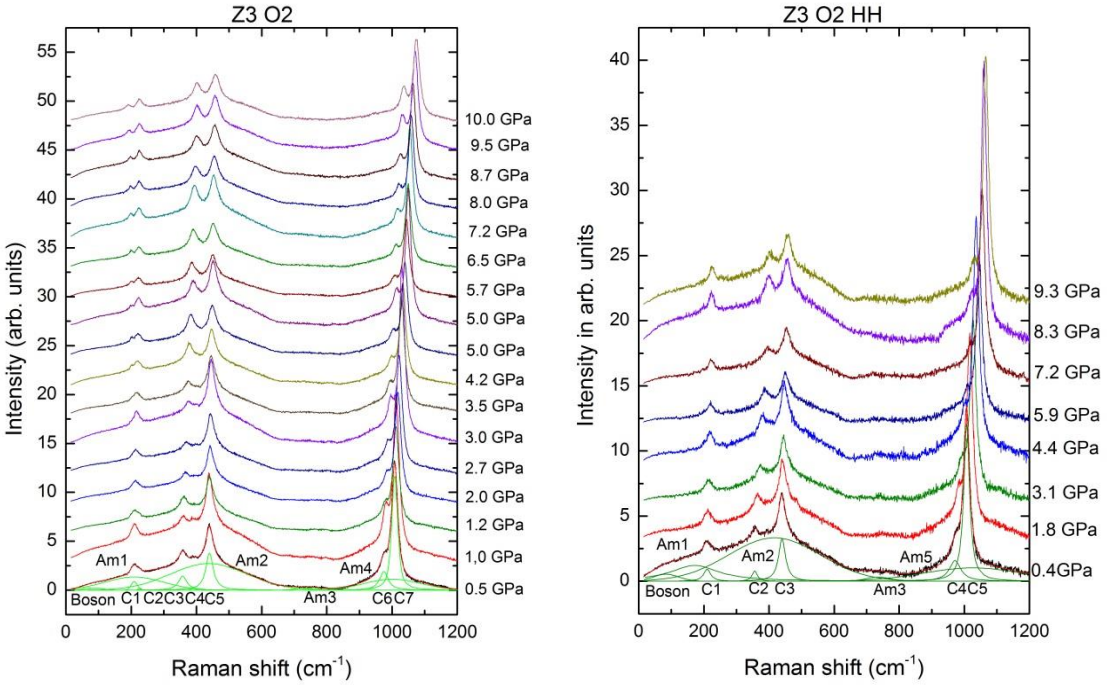

Fig.

Fig. 26: Pressure evolution of the Raman scattering of the heavyly meatmict zircon Z3. The spectrum on left side is one from in-house.

The amorphous peak at 439 cm^{-1} shows a slight increase in wavenumber with pressure. The specimen meassured in the university show a softening between 3 and 6 GPa (Fig. 27a), with a minimum near 5 GPa. The FWHM of the same peak show different behaviour for each specimen (Fig. 27b). The FWHM of the specimen measured additional for DESY has minimum between 4 and 6 GPa. The slope before and after the anomaly is in both cases

high (Fig. 27b, red line). The specimen measured only in house has an anomaly between 3.5 and 6.5 GPa. The FWHM decrease and up to 3.5 GPa, increases after this pressure and have a maximum around 5 GPa (Fig. 27b, indicated by red arrow). After this pressure they decrease again up to 6.5 GPa and remain constant at higher pressure, within the uncertanties (Fig.27b, green line).

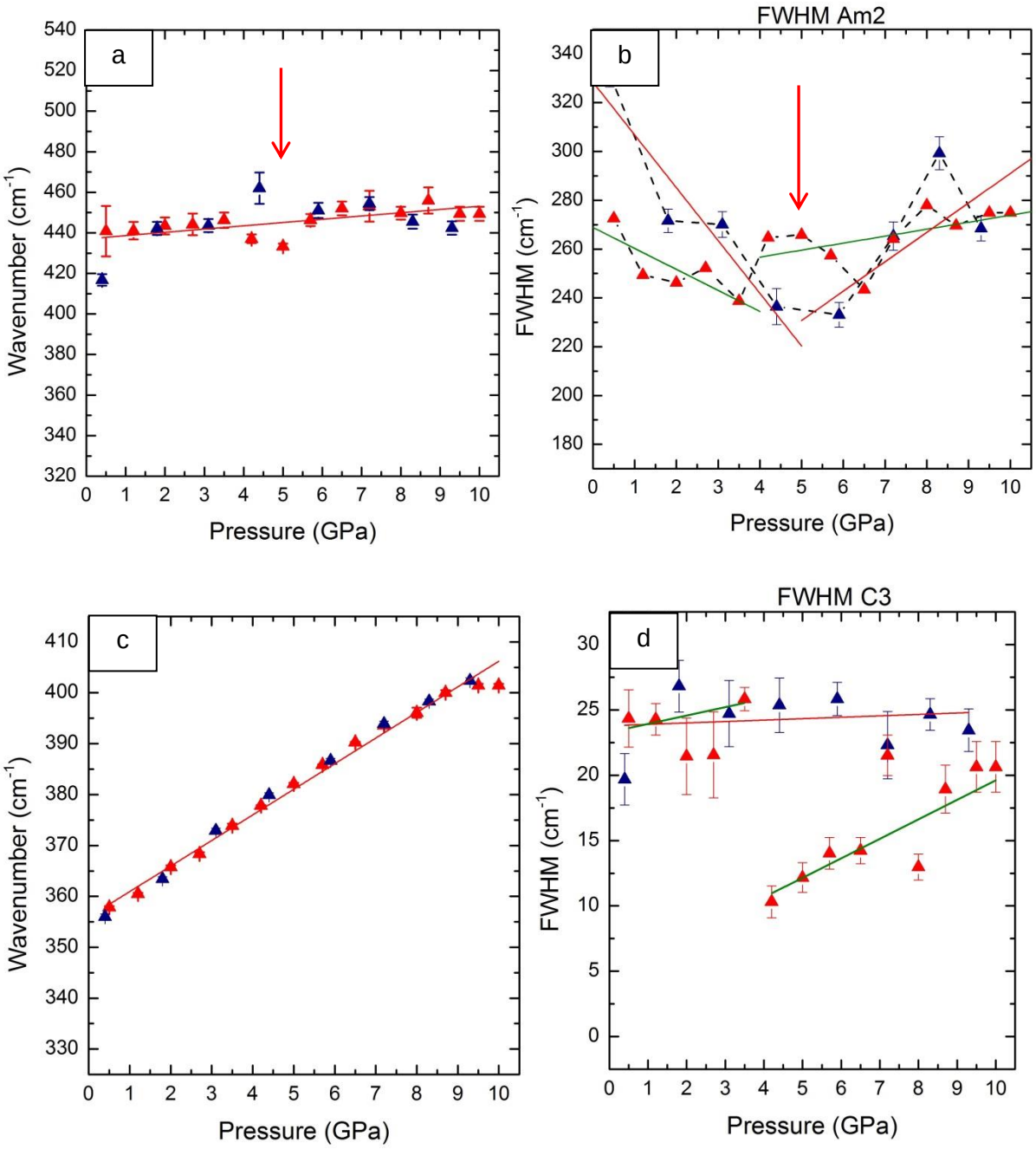

Fig. 27: Pressure dependencies of the wavenumber (a) and FWHM (b) of the SiO4 bending in the amorphous fraction as well as pressure dependencies of the wavenumber (c) and FWHM (d) of the symmetrical SiO_4 anti-symmetrical bending or SiO_4- rotation of the crystalline fraction in sample Z3. The red triangle represents the specimen measured on only in house. The blue triangle represents the specimen measured at DESY. The red line represents the trends of all specimens or when there are anomalies the specimen measured at DESY. The green line represents the trend of the specimen measured in house. The red arrows indicate the point of the anomaly around 5 GPa (a, b)

The crystalline peak at 356 cm^{-1} for the heavy metamict zircon shows a linear increase of the wavenumber by increasing pressure (Fig. 27c). The corresponding FWHM shows an anomaly for the specimen measured in house, near 4 GPa like the FWHM of the amorphous peak at 439 cm^{-1}. The FWHM shows two different ways to accumulate pressure (Fig. 27d). The FWHM of the specimen measured additionally for DESY does not change with pressure. The FWHM of the specimen measured in the university has an anomaly at 4 GPa. It shows a constant trend up to 4 GPa and us then interrupted after exceeding that level of pressure. The FWHM increases again by a smaller FWHM and does not change after this point.

The amorphous peak at 996 cm^{-1} shows in both measured specimen two minima in the plot of the wavenumber dependency on pressure (Fig. 28). For the specimen measured in house the first minimum is at 3 GPa and the second at 4 GPa. The maximum is at 3.5 GPa. After the second minimum at 4 GPa the wavenumber increases with increasing pressure. The specimen measured additionally for DESY has a similar trend as the other specimen. It also reaches its first minimum at 3 GPa and increases up to 4.5 GPa where it has its maximum. The second minimum is at 6 GPa. After this pressure the wavenumber starts to increase again (Fig. 28a, blue triangles). The corresponding plot of the FWHM shows two different trends for both specimens. The FWHM of the specimen measured additionally for DESY show a linear decrease of the FWHM within the uncertainties (Fig28.b, green line). The FWHM of the specimen measured in the university also has two minima. At 3 GPa the first and the second at 4 GPa. The maximum is reached at 3.5 GPa. After the second minimum the FWHM decrease with the same slope with increasing pressure.

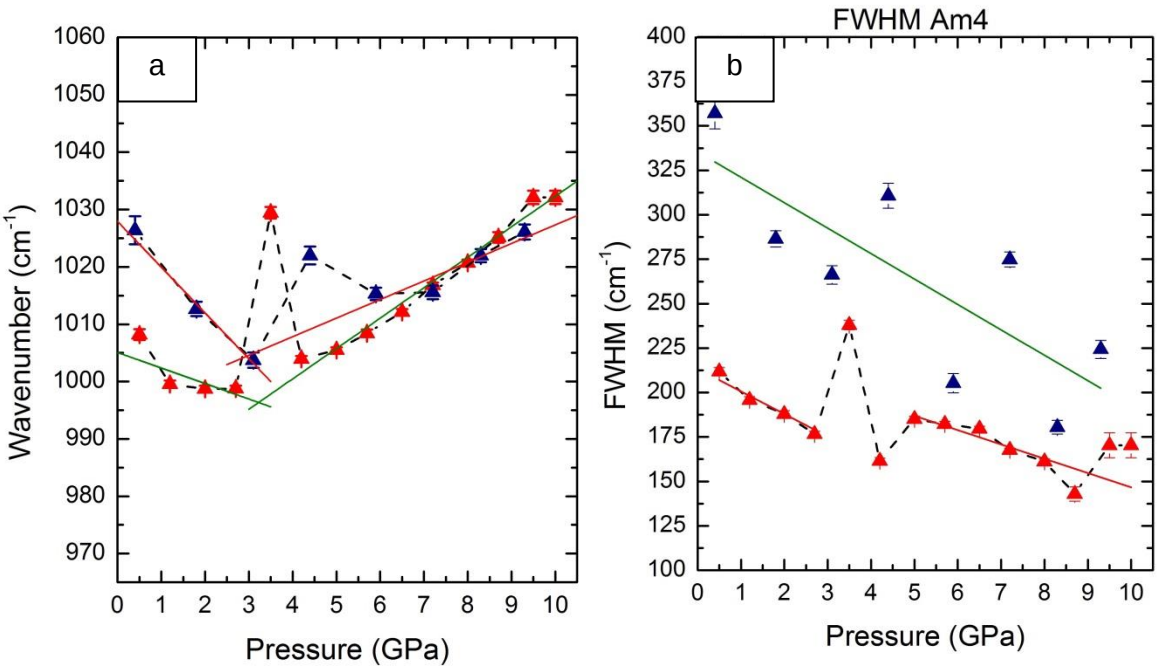

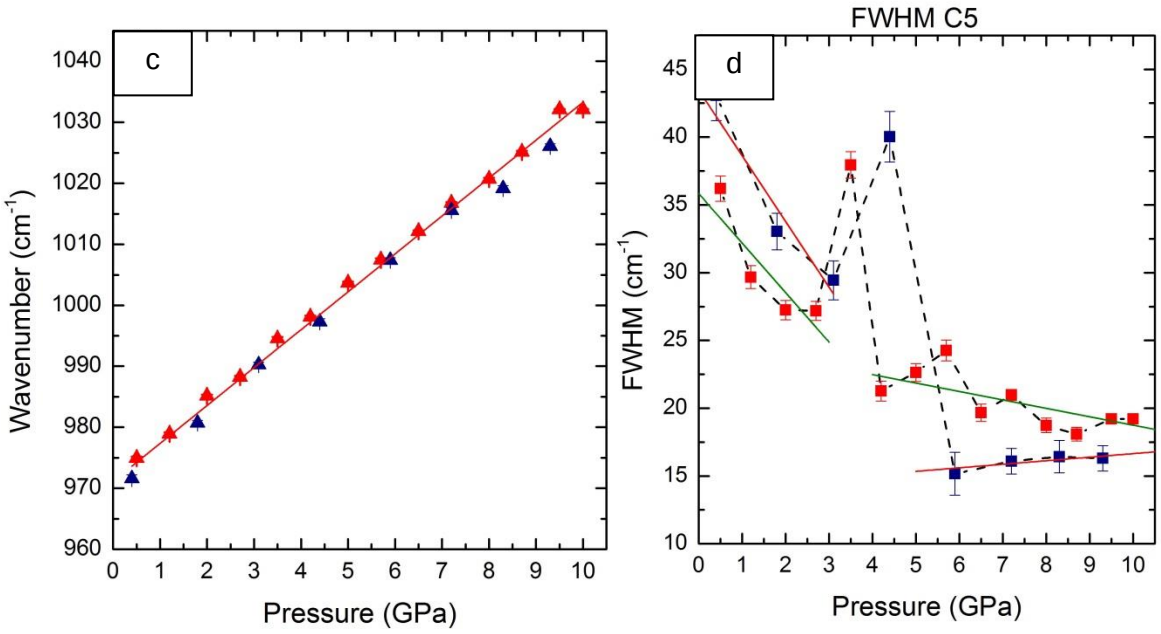

Fig. 28: Pressure dependencies of the wavenumber (a) and FWHM (b) of the SiO4 stretching in the amorphous fraction as well as pressure dependencies of the wavenumber (c) and FWHM (d) of the symmetrical SiO_4 stretching of the crystalline fraction in sample Z3. The red triangle represents the specimen measured on only in house. The blue triangle represents the specimen measured at DESY. The red line represents the trends of all specimens or when there are anomalies the specimen measured at DESY. The green line represents the trend of the specimen measured in house.

The plot of the crystalline peak at 975 cm^{-1} shows a linear increase of the wavenumber with increasing pressure (Fig. 28c). The corresponding plot for the FWHM shows similar trends for both specimens (Fig. 28d). Both have two minima, but at different pressures. They both show their first minima at 3 GPa. The second is for the specimen measured in house at 4 GPa and for the other measured at DESY at 6 GPa. The FWHM for both specimen remains constant after the second minimum.

Therefore these heavy metamict zircons accommodate pressure in two different pathways. The specimen of the additional DESY measurement tries to compensate the pressure by rearranging the amorphous fraction. The specimen measured in house rearranges the amorphous fraction too, but has also to rearrange the crystalline SiO_4 tetrahedra to compensate the pressure. This is due to the inhomogeneous distribution of amorphous fractions in the sample. Homogeneous distribution of amorphous fraction leads to more crystalline structure having to rearrange with increasing pressure. Inhomogeneous distribution leads to more rearrangement of the amorphous fraction with minor changes of the crystalline fraction.

The heavily metamict zircon Z4 was measured only once in house. The pressure evolution of the Raman scattering of the heavily meatmict zircon Z4 shows high intensities for the amorphous- and the boson peak (Fig. 29). The spectrum at 1 GPa was measured on

decompression and the relative intensities differ from the rest of the spectra, most probably because the sample has moved, while decreasing pressure.

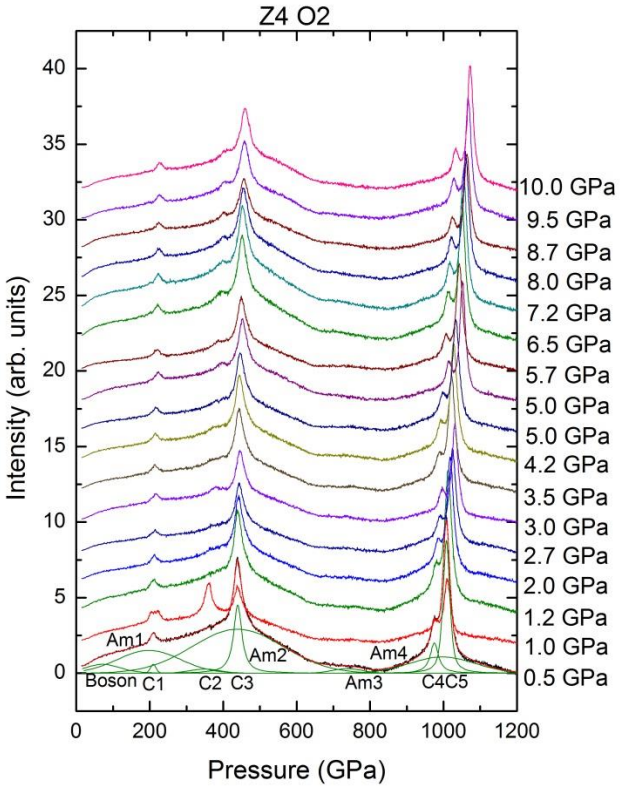

Fig. 29: Pressure evolution of the heavily meatmict zircon Z4.The spectrum at 1 GPa was measrued by decompression and is different due to the fact that the sample moved while decompressing.

The amorphous peak at 439 cm^{-1} shows a linear increase of the wavenumber with increasing pressure (Fig. 30a). The corresponding plot for the FWHM shows an anomaly at 3.5 GPa (Fig. 30b). The FWHM decrease with pressure till 4 GPa (Fig. 30b, red line) and remain constant after 3.5 GPa, within the uncertainties (Fig. 30b, blue line).

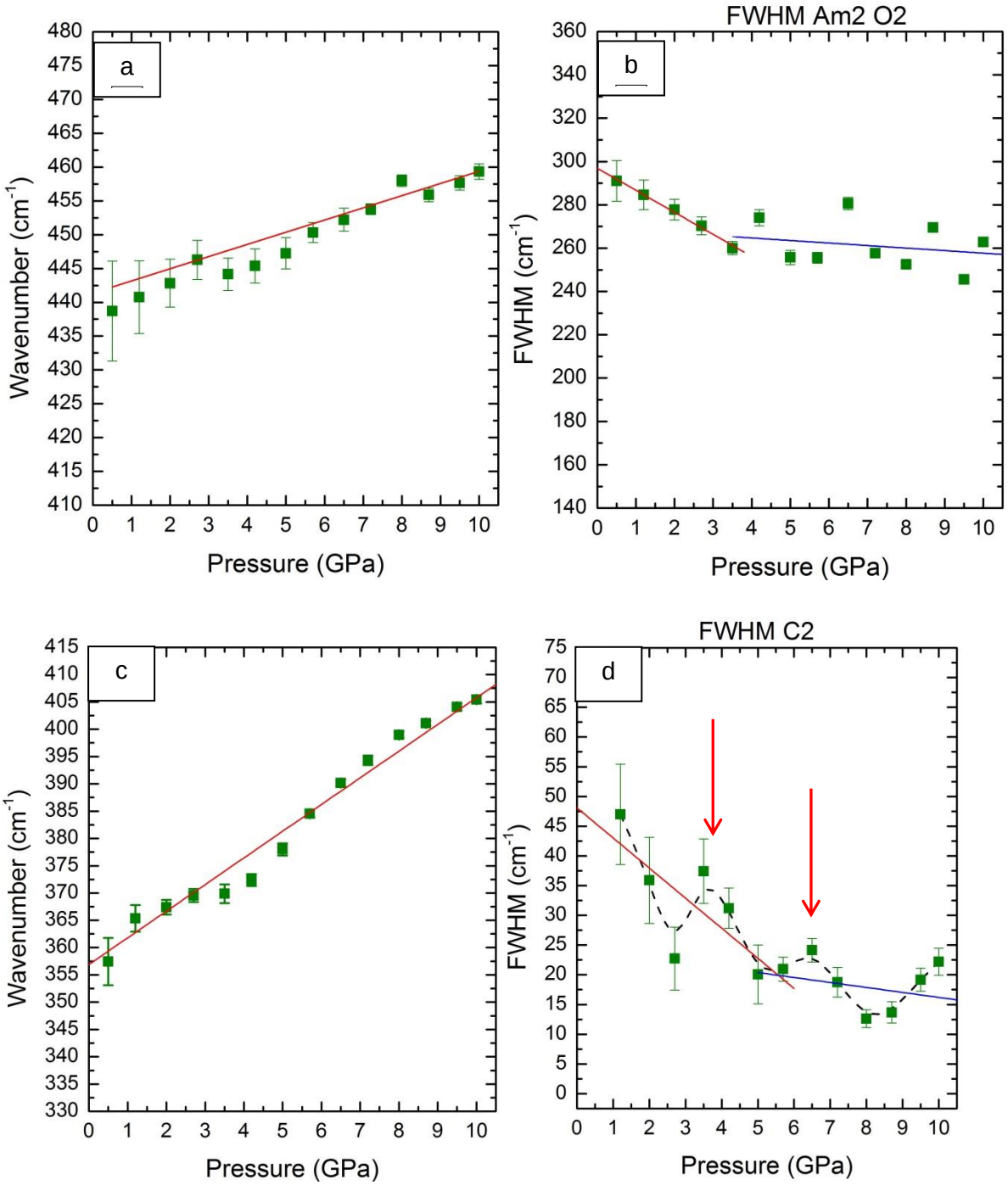

Fig. 30: Pressure dependencies of the wavenumber (a) and FWHM (b) of the SiO4 bending in the amorphous fraction as well as pressure dependencies of the wavenumber (c) and FWHM (d) of the symmetrical SiO_4 anti-symmetrical bending or SiO_4- rotation of the crystalline fraction in sample Z4. The green squares represent the specimen measured in house. The red line represents the overall trend or when there are anomalies its starts with a red line and after an interruption or a minimum it goes on with a blue line. The red arrows indicate the two maxima in the FWHM of the crystalline peak at 356 cm^{-1} (d).

The plot of the crystalline peak at 356 cm^{-1}, showing the wavenumber plotted against pressure, shows a linear increasing trend by increasing pressure. There are also some anomalies between 3 and 6 GPa (Fig. 30c). The plot of the FWHM of the crystalline peak at 356 cm^{-1} shows a linear decrease till 5.5 GPa (Fig. 30d, red line) and is constant above this

pressure (Fig. 30d, blue line). Additionally two maxima occur at 3.5 GPa and around 6.5 GPa (Fig. 30d, indicated with red arrows)

The amorphous peak at 996 cm^{-1} shows a linear trend of increasing wavenumbers with increasing pressure. There are also some outbreaks between 3 and 6 GPa (Fig. 31a). The FWHM of this peak has an anomaly at 6.5 GPa (Fig. 31b). It decreases with increasing pressure and interrupt at 6.5 GPa. After this point it shows a sharper peak that does not change with pressure.

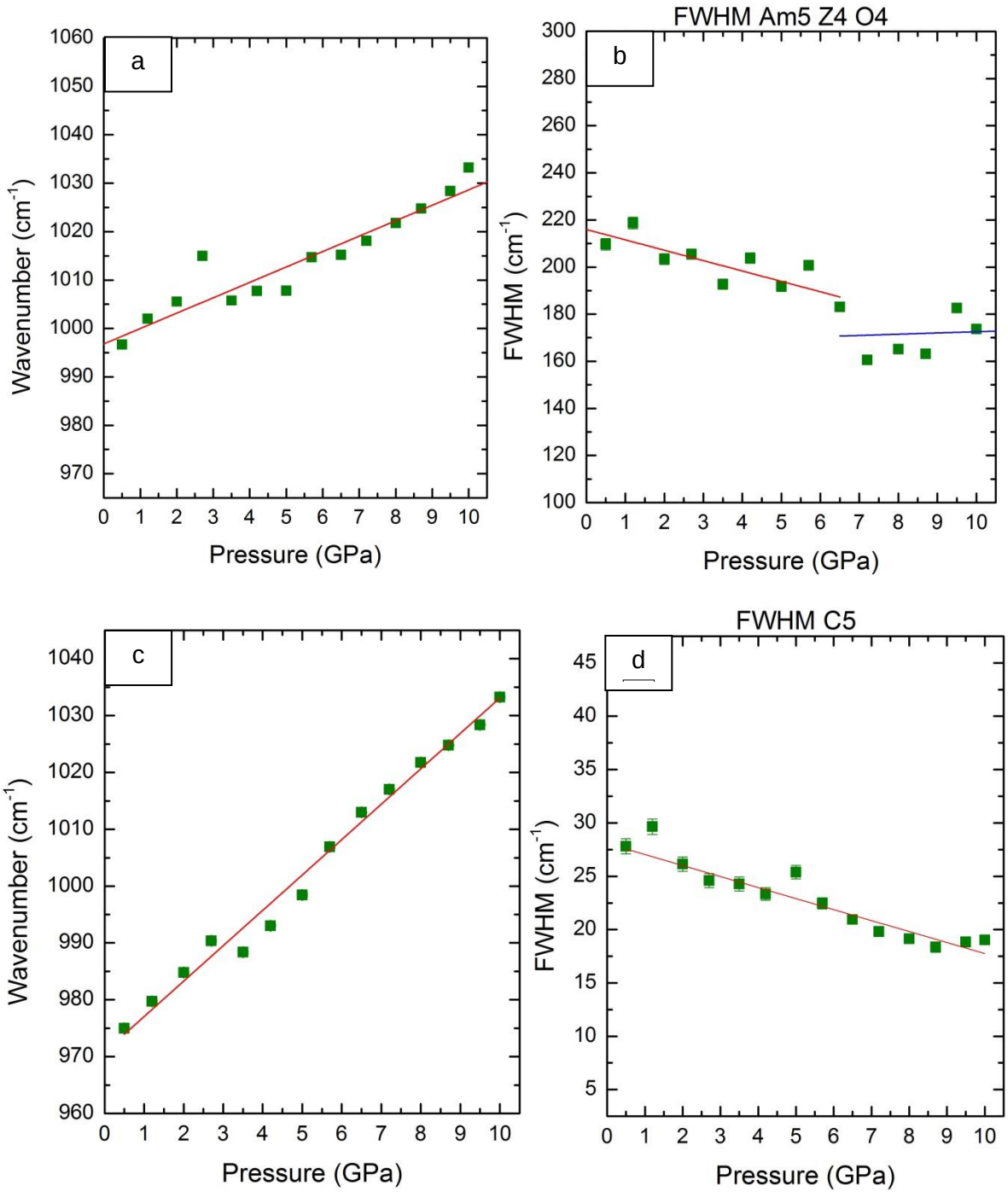

Fig.32: Pressure dependencies of the wavenumber (a) and FWHM (b) of the SiO4 stretching in the amorphous fraction as well as pressure dependencies of the wavenumber (c) and FWHM (d) of the symmetrical SiO_4 stretching of the crystalline fraction in sample Z4. The green squares represent the specimen measured in house. The red line represents the overall trend or when there are anomalies its starts with a red line and after an interruption or a minimum it goes on with a blue line.

The crystalline peak at 975 cm^{-1} shows a linear increase of the wavenumber in alignment with increasing pressure (Fig. 31c). Only between 3 and 6 GPa seems to be an interruption. The slope is the same but the wavenumbers are below the trendline. The FWHM of the crystalline peak at 975 cm^{-1} shows a linear decrease of the FWHM. Two points seem to break out of the alignment but their positions are still in the range of mechanical errors, which allows a linear interpretation (Fig. 31d).

In summary, the heavily metamict zircon Z4 seems to rearrange equally in the amorphous and the crystalline fraction to accumulate pressure. The changes of the FWHM for the peak at 356 cm^{-1} seem to react to the anomaly of the amorphous peaks at 439 cm^{-1} and 996 cm^{-1}. Traces of these changes can be seen in every plot of wavenumbers against pressure.

To understand what happens under pressure with the zircon compressibility can be determined. The isothermal volume compressibility β is defined as the change in the unit cell volume V with change in pressure p at constant temperature T:

$$\beta = -\frac{1}{V_0} \cdot \left(\frac{\partial V}{\partial p}\right)_T$$

, where V_0 is the unit-cell volume at zero pressure.

The plots of the wavenumber against pressure also carry information about the compressibility of the structure, on particular about the stiffness of the corresponding vibrational species. This one can define “phonon” compressibility:

$$\beta_\omega = -\frac{1}{\omega_0} \cdot \frac{d\omega}{dp}$$

Most of the ω(p) trends can be fitted by a linear function:

$$\omega(p) = \omega_0 + \frac{d\omega}{dp}$$

p and thus the parameters w_0 and dω/dp can be determined.

A larger slope describes that it is easier to compress. The following tables (Table 6, 7, and 8) are the crystalline peaks in order of increasing wavenumbers.

Sample	$(1/\omega_0 \times d\omega/dP) \times 100$	$\pm(1/\omega_0 \times d\omega/dP) \times 100$	$(1/\omega_0 \times d\omega/dP) \times 100$	$\pm(1/\omega_0 \times d\omega/dP) \times 100$	$1(1/\omega_0 \times d\omega/dP) \times 100$	$\pm(1/\omega_0 \times d\omega/dP) \times 100$	$(1/\omega_0 \times d\omega/dP) \times 100$	$\pm(1/\omega_0 \times d\omega/dP) \times 100$
	For 356 cm^{-1}		For 440 cm^{-1}		For 976 cm^{-1}		1008 cm^{-1}	
unit	(GPa^{-1})	(GPa^{-1})	(GPa^{-1})	(GPa^{-1})	(GPa^{-1})	(GPa^{-1})	(GPa^{-1})	(GPa^{-1})
Z7	1.17	0.009	0.31	0.01	0.5	0.004	0.535	0.004
Z1	1.43	0.03	0.43	0.02	0.56	0.01	0.621	0.005
Z3	1.4	0.03	0.462	0.007	0.64	0.01	0.687	0.007
Z4	1.46	0.06	0.5	0.02	0.64	0.02	0.7	0.02

Table 6: Compressibility of crystalline peaks in order of increasing wavenumbers.

Table 6 shows the compressibility of the crystalline peaks. The compressibility of all crystalline peaks increases with the degree of metamictization. Table 8 shows the compressibility of the amorphous peak at 439 cm^{-1}.

Sample	$(1/\omega_0 \times d\omega/dP) \times 100$	$\pm(1/\omega_0 \times d\omega/dP) \times 100$
unit	(GPa^{-1})	(GPa^{-1})
Z1 DESY	0.42	0.02
Z1 uni	0.5	0.3
Z3	0.4	0.1
Z4	0.41	0.07

Table 7: Compressibility of the metamict peak at 439 cm^{-1}.

The amorphous peak at 439 cm^{-1} has a compressibility of 0.5 GPa^{-1} x 100 within the uncertainties, independent of the degree of metamictization. Table 8 shows the amorphous at 996 cm^{-1}.

Sample	$(1/\omega_0 \times d\omega/dP) \times 100$	$\pm(1/\omega_0 \times d\omega/dP) \times 100$
unit	(GPa^{-1})	(GPa^{-1})
Z1 DESY	0.53	0.09
Z1 Uni	0.42	0.08
Z3 DESY	0.32	0.09
Z3 Uni	0.54	0.03
Z4	0.32	0.04

Table 8: Compressibility of the metamict peas at 996 cm^{-1}.

The amorphous peak at 996 cm^{-1} has a compressibility between 0.35 and 0.5 GPa^{-1} x 100. This peak´s compressibility seems to be independent from the total degree of metamictization and shows higher sensitivity for local structural defects. The values for these calculations can be found in the appendix.

In Fig. 32 the normalized intensity of the total amorphous fraction is plotted against pressure. The behavior of heavily and moderately metamict zircons shows no pressure induced change within the errors. The approximate value of amorphous fractions of the heavily metamict zircons is around 70% of the sample and in the intermediately metamict zircon around 40%. This shows that with rising degree of metamictization the amorphous fraction increases in the sample.

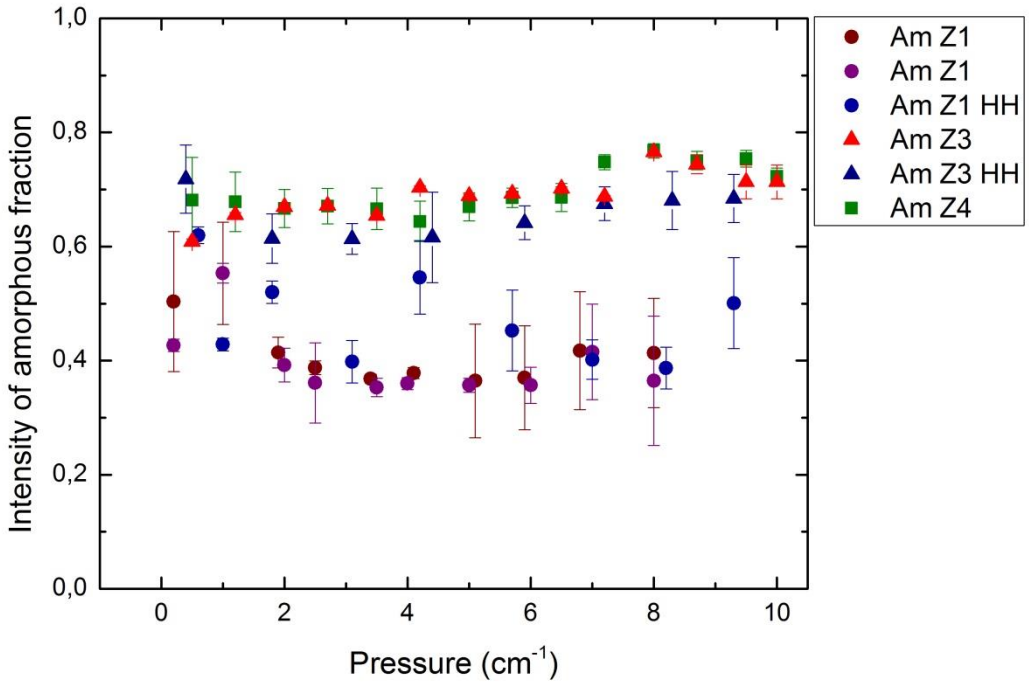

Fig.32: Normalized Intensity of the all amorphous fractions versus Pressure.

Conclusions

The main results of this study are as follows:

It is demonstrated that

- In-situ high-pressure Raman spectrocopy can distinguish between the response of the crystalline and amorphous fraction to elastic stress.
- The compressibility of the crystalline fraction increases with the degree of radiation-induced structural damage, whereas the compressibility of the amorphous fraction is independent of the degree of metamictization.
- The amorphous fraction can be determined by the relative integrated intensities of the Raman peaks originated from the amorphous and the crystalline fraction. As expected, the amorphous fraction increases with the radiation dose. However within uncertanties, the amorphous fraction does not change with pressure.
- Although all studied samples are chemically homogenious. The moderately and heavily metamict zircons samples show two possible pathways for the structure to accommodate pressure:

    - by distorting the SiO_4 tetrahedra only in the amorphous fraction.

    - by rearranging SiO_4 in both the amorphous and the crystalline fractions.

- Regardless of the pathway, the Raman data reveal pressure-induced structural softening between 3 and 6 GPa. This is due to the weakening in the Si-O bond strength in the amorphous regions accompanied by damping of the SiO_4 stretching in the crystalline region, The weakening of the Si-O bonds is caused by an increase in the Si coordination from 4 to 5 or 6 as theoretically predicted by Trachenko [1].
- Measurements on decompression show that the pressure induced structural changes are not entirely reversible, most probably due to irreversible change local atomic surroundings in the amorphous nanoregions.

References

[1] Trachenko, K., Brrazhkin, V. V., Tsoik, O. B., Dove M. T. and Salje, E. K. H. (2007): Pressure-Induced Structural Transformation in Radiation-Amorphized Zircon. In Phys. Rev. Letters, PRL **98**, 135502

[2] Scherer, E., Whitehouse, M. J. and Münker, C. (2007): Zircon as a Monitor of Crustal Growth. Elements, **3**, 19-30.

[3] Harley. S.L, and Kelly, N. M (2007): Zircon Tiny but Timely. Elements, **3**, 13-18.

[4] Geisler, T., Schlategger, U. and Tomaschek, F. (2007): Re-equilibration of Zircon in aqueous fluids and melts. Elements, **3**, 43-50.

[5] Tomasic, N., Bermanec, V., Gajovic, A., and Linaric, M.R. (2008): Metamict Mienrals: an Insight into a Relic Crystal Structure Using XRD, Raman Spectroscopy, SAED and HRTEM. CROATICA CHEMICA ACTA, CCACAA, **81** (2), 391-400, ISSN-0011-1643, CCA-3256

[6] Geisler, T. Rashwan, A.A., Rahn, M.K.W, Poller, U., Zwingmann, H. Pidgeon, R.T., Schleicher, H., Tomaschek, F.(2003): Low-temperature hydrothermal alteration of natural metamict zircons from the Eastern Desert. Egypt Mineralogical Magazine 76: 485-508.

[7] Speer, J.A., Cooper, B.N. (1982): Crystal structure of synthetic hafnon, HfSiO4, comparison with zircon and the actinide orthosilicates. Am Mineral 67:804-808

[8] Hoekstra HR, Fuchs LH (1956): Synthesis of coffinite-USiO4. Science 123:105

[9] Fuchs LH, Gebert E (1958): X-ray studies of synthetic coffinite, thorite and uranothorites. Am Mineral 43:243-248

[10] Ni, Y., Hughes, J.M., Mariano, A.N. (1995): Crystal chemistry of the monazite and xenotime structures. Am Mineral 80:21-26

[11] Finch, R. J. and Hanchar, J. M.(2003): Structure and chemistry of zircon and zircon materials. Rev. Min. and Geochem., January 2003, v. 53, pp 1-25, doi:10.2113/0530001

[12] L. M.Wang, R. K. Eby, J. Janeczek, and R. C. Ewing, Nucl. Instr. Meth. **B 59/60** (1991) 395–400

[13] Ríos, S., Malcherek, T., Salje, E.K.H., Domeneghetti, C., (2000): Localized defects in radiation-damaged zircon. Acta Crystallogr B 56:947-952

[14] Kittle, E and. Williams, Q. (1993): Observation of the zircon to scheelite transition at 300 K. In American Mineralogist, Volume **78**, pages 245-252

[15] Long, Y. W., Yang, L. X., Yu, Y., Li, F. Y., Lu, Y. X., Yu, R. C. Liu, Y. L., and Jin, C. Q. (2008): High-pressure Raman scattering study on zircon- to scheelite-type structural phase transitions of RCrO4. *J. Appl. Phys.* **103**, 093542

[16] Ríos, S. and Boffa-Ballaran, T. (2003): Microstructure of radiation-damaged zircon under pressure. *J. Appl. Cryst.*, **36**, 1006-1012

[17] Nasdala, L., Miletich, R. and Ruschel, K. (2008): Raman study of radiation-damaged zircon under hydrostatic compression. Published online since 21.08.2008 © Springer-Verlag.

[18] Kröner, A. and William, I. S. (1993): Age of Metamorphism in the High-Grade Rocks of Sri Lanka. The Journal of Geology Vol. 101,**4** , pp. 513-521

[19] Stutzer, O. and Eppler, W.F. (1935): Die Lagerstätten der Edelsteine und Schmucksteine. Berlin: Borntraeger

[20] Gmelin, L. (2013): Zirkonium, Springer-Verlag

[21] Carter, A. and Bristow, C. S. (2003): Linking hinterland evolution and continental basin sedimentation by using detrital zircon thermochronology: a study of the Khorat Plateau Basin, eastern Thailand. Basin Research Volume 15, Issue 2, pages 271–285

[22] Giacovazzo, C., Monaco, H. L., Artioli, G., Viterbo, D., Milanesio, M., Ferraris, G., Gilli, G., Giili, P., Zanotti, G. Catti, M. (2002): Fundamentals of Crystallography, Oxford, Third edition, pp 158

[23] http://kristall.uni-mki.gwdg.de/Docs/Ausstattung/puldiff.html (March 2015)

[24] Chatterjee, N. (2012): Electron Microprobe Analysis, MIT, Cambridge, MA, USA

[25] http://probelab.geo.umn.edu/electron_microprobe.html (March 2015)

[26] Smith, G., Dent, W.E. (2005): Modern Raman spectroscopy a practical approach. Chichester John Wiley and Sons Ltd. p.73

[27] Kolesov, B.A. Geiger, C.A. and Armbruster, T. (2001): The dynamic properties of zrircon studied by single-crystal X-ray diffraction and Raman spectroscopy. Eur. J. Mineral. **13**, 939-948

[28] Dawson, P., HARGREAVE, M. M. and WILKINSON, G.R. (1970): The vibrational spectrum of zircon (ZrSiO,). J. Phys. C: Solid St. Phys., 1971, Vol. **4.** Printed in Great Britain

[29] Welsch, A.-M. (2009): High-pressure Raman scattering of pure and doped PbSc0.5Ta0.5O3 and PbSc0.5Nb0.5O3 single crystals, PhD thesis, University of Hamburg.

[30] Angel, R.J., Bujak, M., Zhao, J., Gatta, G.D. and Jacobsen, S.D. (2006): Effective hydrostatic limits of pressure media for high-pressure crystallographic studies. J. Appl. Cryst., ISSN 0021-8898.

[31] Eggert, J.H., Goettel, K.A. and Silvera I.F., (1989): Phys. Rev. B **40**, 5724

[32] Eggert, J.H., Goettel, K.A. and Silvera I.F., (1989): Phys. Rev. B **40**, 5733

[33] Eggert, J.H., Moshry, F., Evans, W.J., Goettel, K.A. and Silvera, I.F., (1991): Phys. Rev., B **44**, 7202

[34] Syassen, K. (2008): High Pres Res **28**, 75

[35] Mao, H.K., Xu, J. and Bell, P.M.(1986): J. Geophys. *Res* B **91**, 4673

[36] Piermarini. G.J., Block, S., Barnett, J.D. and Forman, R.A. (1975): J. Appl. Phys. **46**, 2774

[37] Barnett, J.D., Block, S. and Piermarini G.J. (1973): Rev Sci Instrum **44**, 1

[38] Vos W.L. and Schouten J.A., (1991): J. Appl. Phys. **69** 6744

[39] Milletich, R., Allan, D.A. and Kuhs, W.F. (2000): Reviews in Mineralogy and Geochemistry **41**,499

[40] Geisler T. and Pidgeon R.T. (2002) Raman scattering from metamict zircon: Comments on “Metamictization of natural zircon: accumulation versus thermal annealing of radioactivity-induced damage” by Nasdala et al., 2001 (Contributions to Mineralogy and Petrology, 141, 125-144). Contrib. Mineral. Petrol. 143, 750-755.

[41] http://www.webelements.com/uranium/isotopes.html (March 2015)

[42] Firestone, R.B., Shirley, V.S., Chu, S.Y.F., Baglin, C.M. and Zipkin, J.(1996): Table of Isotopes, John Wiley and Sons, New York.

[43] Steiger, R. H., Jaeger, E. (1977): Subcommision on Geochronology: convention on the use of decay constants in geo- and cosmo-chronology. Earth Planet, Sci. Lett. 36, 359-362.

[44] http://www.ciaaw.org/isotopic-abundances.htm (March 2015)

[45] http://physics.nist.gov/PhysRefData/Compositions/notes.html (March 2015)

[46] Scott, H. P., Williams, Q. and Knittle E. (2001): ltralow Compressibility Silicate without Highly Coordinated Silicon, Phys. Rev. Lett., 88, 015506

[47] Nasdala, L., Miletich, R. and Ruschek, K. (2008): Raman study of radiation-damaged zircon und hydrostatic compression, Phs Cehm Minerals, 35:597-602 DOI 10.1007/s00269-008-0251-5

Appendix

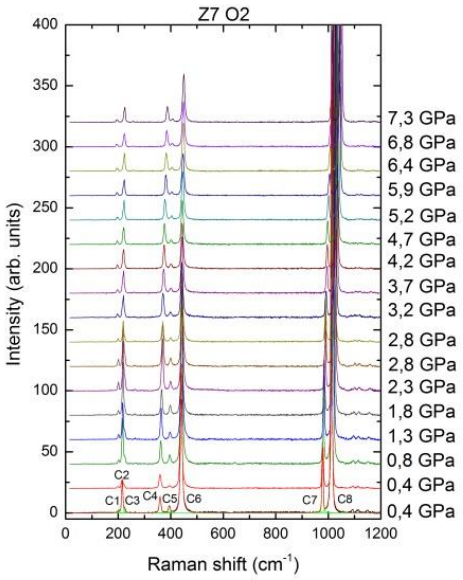
Z7 O2
Intensity (arb. units)
Raman shift (cm-1)
7,3 GPa
6,8 GPa
6,4 GPa
5,9 GPa
5,2 GPa
4,7 GPa
4,2 GPa
3,7 GPa
3,2 GPa
2,8 GPa
2,8 GPa
2,3 GPa
1,8 GPa
1,3 GPa
0,8 GPa
0,4 GPa
0,4 GPa
C1 C2 C3 C4 C5 C6 C7 C8

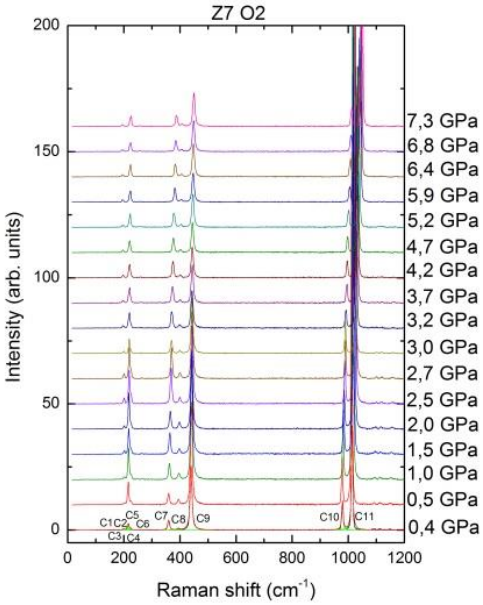
Z7 O2
Intensity (arb. units)
Raman shift (cm-1)
7,3 GPa
6,8 GPa
6,4 GPa
5,9 GPa
5,2 GPa
4,7 GPa
4,2 GPa
3,7 GPa
3,2 GPa
3,0 GPa
2,7 GPa
2,5 GPa
2,0 GPa
1,5 GPa
1,0 GPa
0,5 GPa
0,4 GPa
C1 C2 C3 C4 C5 C6 C7 C8 C9 C10 C11

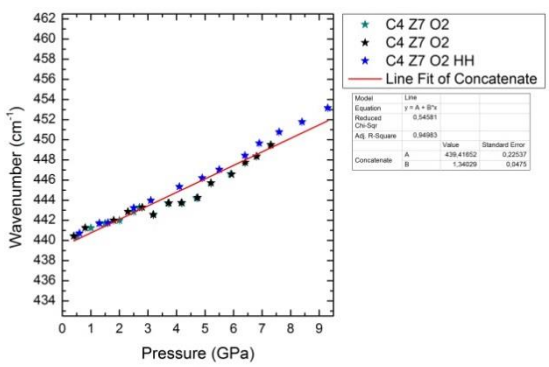
C4 Z7 O2
C4 Z7 O2
C4 Z7 O2 HH
Line Fit of Concatenate
Wavenumber (cm-1)
Pressure (GPa)

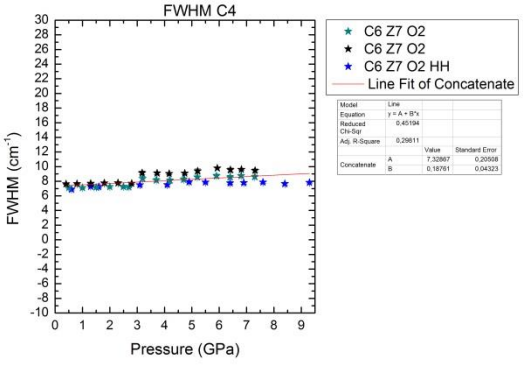
FWHM C4
C6 Z7 O2
C6 Z7 O2
C6 Z7 O2 HH
Line Fit of Concatenate
FWHM (cm-1)
Pressure (GPa)

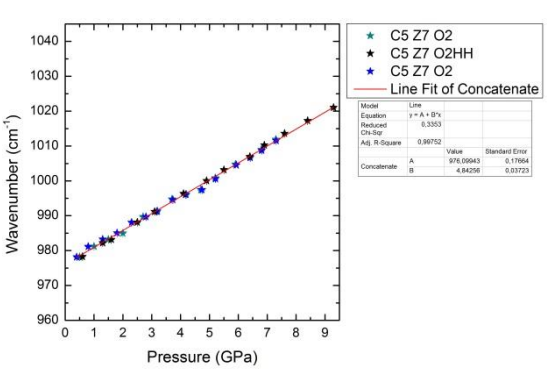
C5 Z7 O2
C5 Z7 O2HH
C5 Z7 O2
Line Fit of Concatenate
Wavenumber (cm-1)
Pressure (GPa)

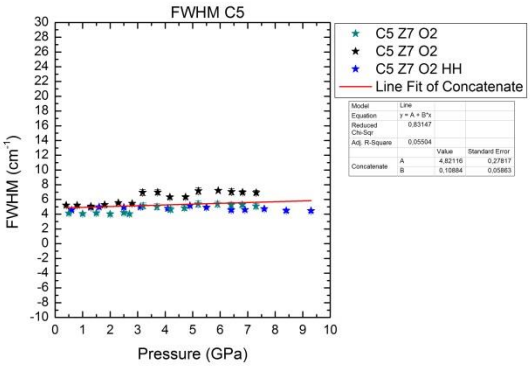
FWHM C5
C5 Z7 O2
C5 Z7 O2
C5 Z7 O2 HH
Line Fit of Concatenate
FWHM (cm-1)
Pressure (GPa)

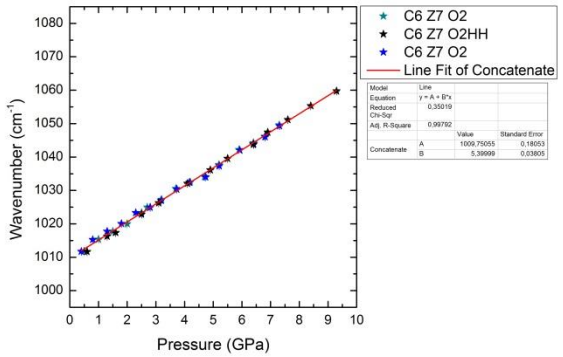
C6 Z7 O2
C6 Z7 O2HH
C6 Z7 O2
Line Fit of Concatenate
Wavenumber (cm-1)
Pressure (GPa)

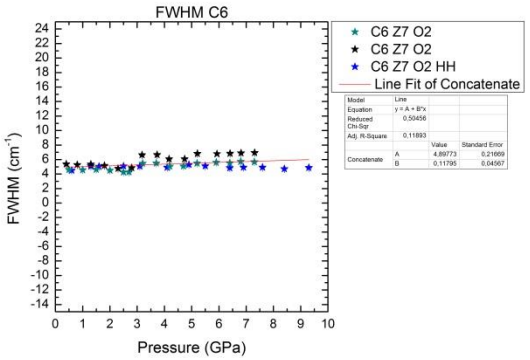
FWHM C6
C6 Z7 O2
C6 Z7 O2
C6 Z7 O2 HH
Line Fit of Concatenate
FWHM (cm-1)
Pressure (GPa)

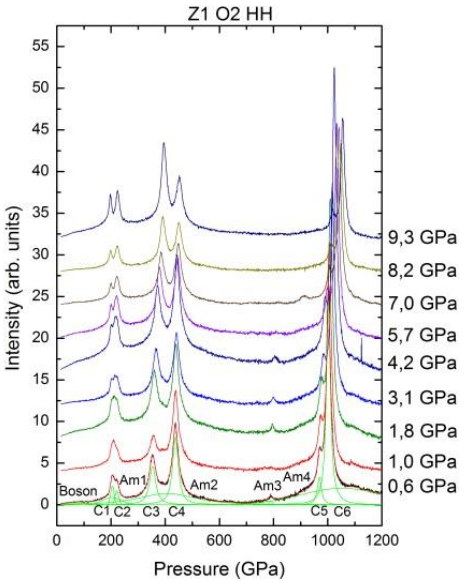
Z1 O2 HH
Intensity (arb. units)
9,3 GPa
8,2 GPa
7,0 GPa
5,7 GPa
4,2 GPa
3,1 GPa
1,8 GPa
1,0 GPa
0,6 GPa
Boson
Am1
Am2
Am3
Am4
C1 C2 C3 C4
C5 C6
Pressure (GPa)

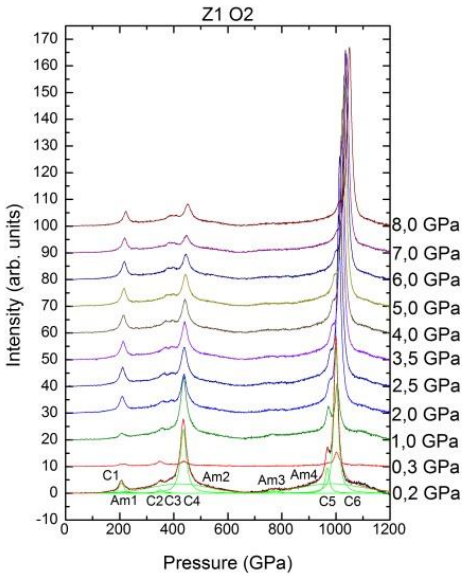
Z1 O2
Intensity (arb. units)
8,0 GPa
7,0 GPa
6,0 GPa
5,0 GPa
4,0 GPa
3,5 GPa
2,5 GPa
2,0 GPa
1,0 GPa
0,3 GPa
0,2 GPa
C1
Am1 C2C3 C4
Am2
Am3 Am4
C5 C6
Pressure (GPa)

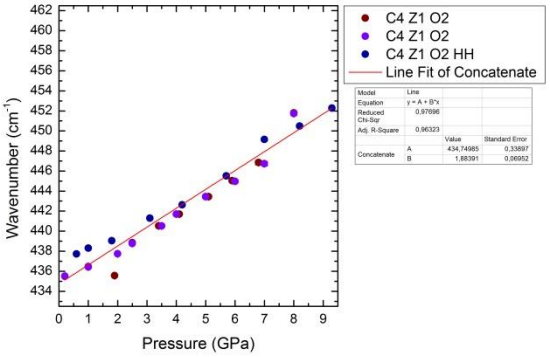
C4 Z1 O2
C4 Z1 O2
C4 Z1 O2 HH
Line Fit of Concatenate
Wavenumber (cm-1)
Pressure (GPa)

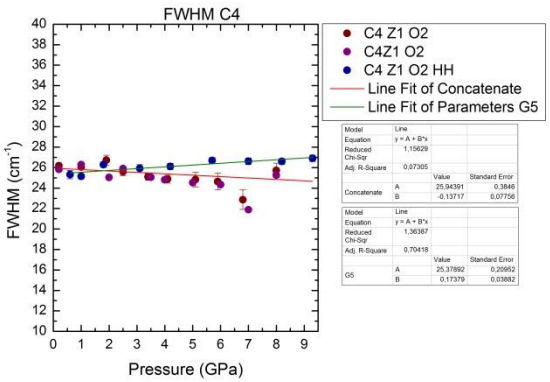
FWHM C4
C4 Z1 O2
C4Z1 O2
C4 Z1 O2 HH
Line Fit of Concatenate
Line Fit of Parameters G5
FWHM (cm-1)
Pressure (GPa)

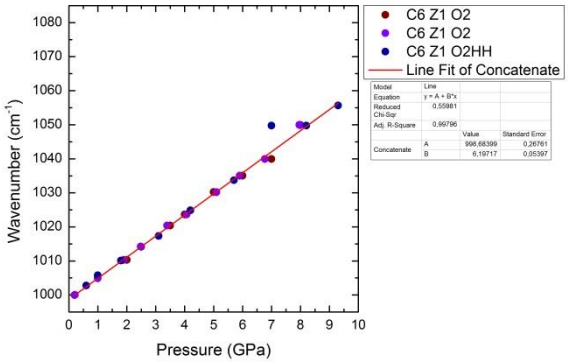
C6 Z1 O2
C6 Z1 O2
C6 Z1 O2HH
Line Fit of Concatenate
Wavenumber (cm-1)
Pressure (GPa)

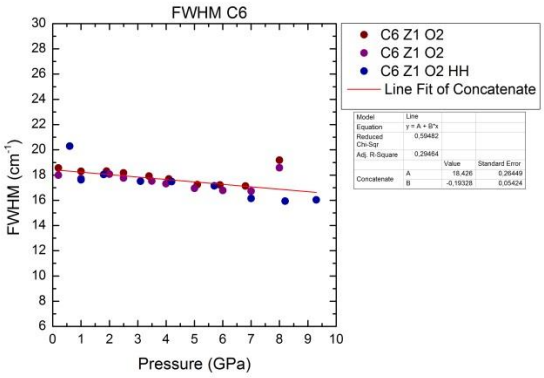
FWHM C6
C6 Z1 O2
C6 Z1 O2
C6 Z1 O2 HH
Line Fit of Concatenate
FWHM (cm-1)
Pressure (GPa)

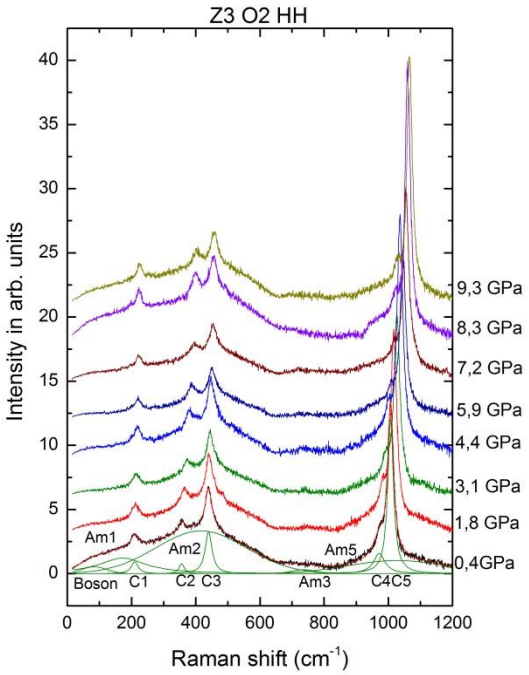
Z3 O2 HH
Intensity in arb. units
9,3 GPa
8,3 GPa
7,2 GPa
5,9 GPa
4,4 GPa
3,1 GPa
1,8 GPa
0,4GPa
Am1
Am2
Am5
Boson
C1
C2 C3
Am3
C4C5
Raman shift (cm-1)

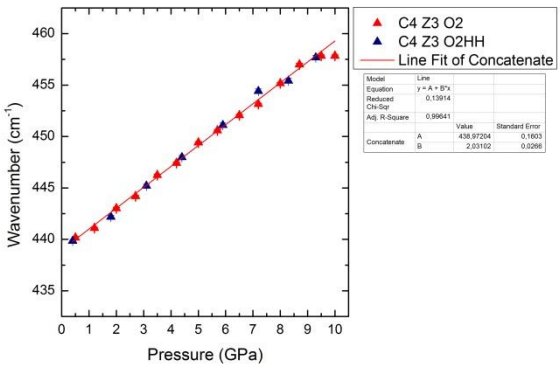
C4 Z3 O2
C4 Z3 O2HH
Line Fit of Concatenate
Wavenumber (cm-1)
Pressure (GPa)

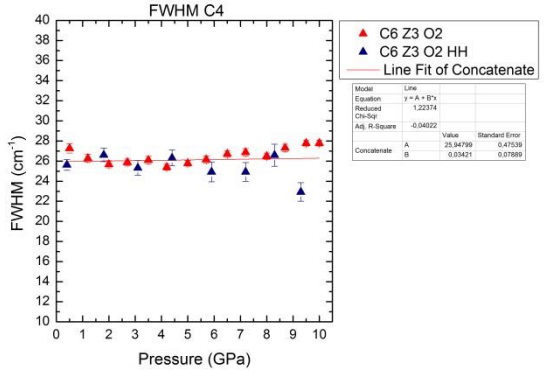
FWHM C4
C6 Z3 O2
C6 Z3 O2 HH
Line Fit of Concatenate
FWHM (cm-1)
Pressure (GPa)

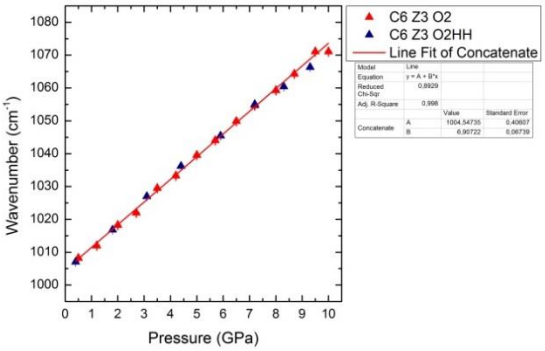

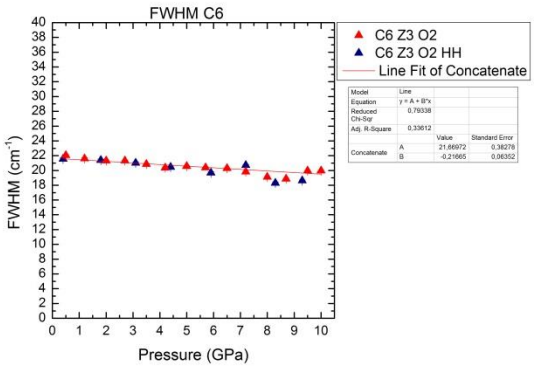

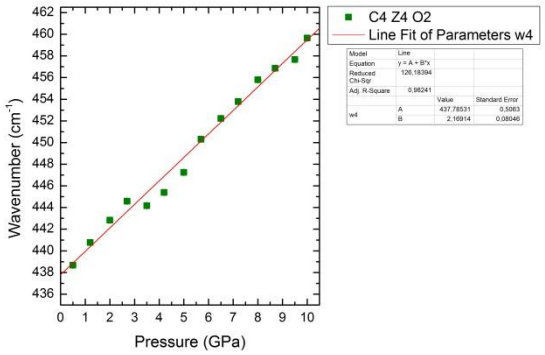

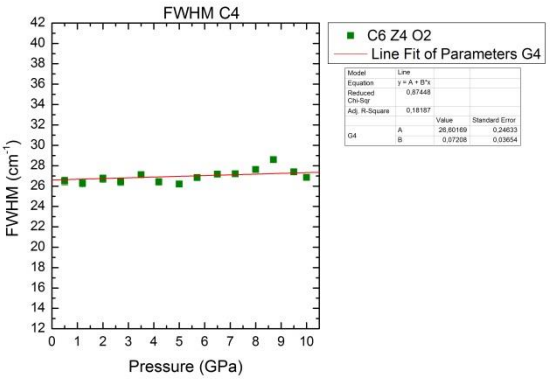

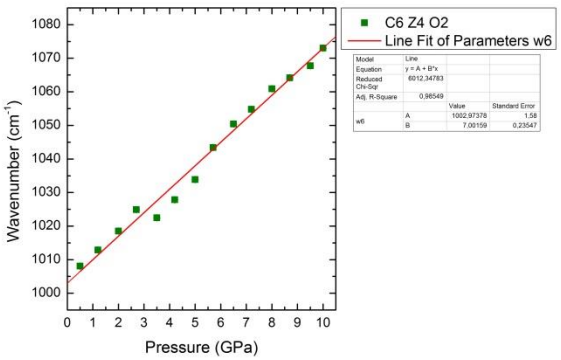

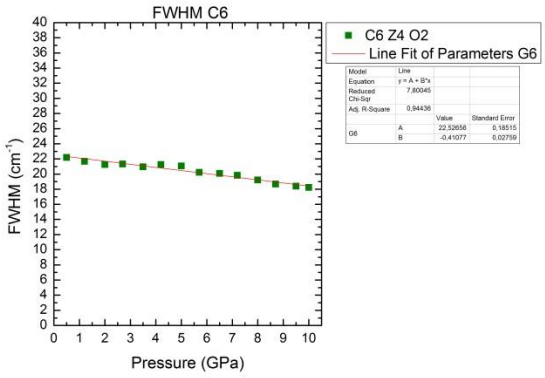

C4 (ω: 440 cm^{-1})

Sample	ω_0	$\pm\omega_0$	$d\omega/dP$	$\pm d\omega/dP$
	(cm^{-1})	(cm^{-1})	(GPa^{-1})	(GPa^{-1})
Z7	439.4	0.2	1.34	0.05
Z1	434.7	0.3	1.88	0.07
Z3	439	0.2	2.03	0.03
Z4	437.8	0.5	2.17	0.08

C2 (ω: 356 cm^{-1})

Sample	ω_0	$\pm\omega_0$	$d\omega/dP$	$\pm d\omega/dP$

	(cm^{-1})	(cm^{-1})	(GPa^{-1})	(GPa^{-1})
Z7	358.2	0.2	4.19	0.03
Z1	350.1	0.5	5	0.1
Z3	355.9	0.7	5	0.1
Z4	356	2	5.2	0.2

C5 (ω 978 cm^{-1})

Sample	**ω_0**	**$\pm\omega_0$**	**$d\omega/dP$**	**$\pm d\omega/dP$**
	(cm^{-1})	(cm^{-1})	(GPa^{-1})	(GPa^{-1})
Z7	976.1	0.2	4.84	0.04
Z1	966	0.5	5.43	0.09
Z3	971.1	0.6	6.2	0.1
Z4	971	1	6.2	0.2

C6 (ω 1011 cm^{-1})

Sample	**ω_0**	**$\pm\omega_0$**	**$d\omega/dP$**	**$\pm d\omega/dP$**
	(cm^{-1})	(cm^{-1})	(GPa^{-1})	(GPa^{-1})
Z7	1009.8	0.2	5.4	0.04
Z1	998.7	0.3	6.2	0.05
Z3	1004.5	0.4	6.91	0.07
Z4	1003	2	7	0.2

Am2 (ω 439)

Sample	**ω_0**	**$\pm\omega_0$**	**$d\omega/dP$**	**$\pm d\omega/dP$**
	(cm^{-1})	(cm^{-1})	(GPa^{-1})	(GPa^{-1})
Z1 DESY	435.5	0.5	1.82	0.09
Z3	437	3	1.6	0.6
Z4	441	2	1.8	0.3

Sample	**P_{an}**	**$\omega_0<P_{an}$**	**$\pm\omega_0<P_{an}$**	**$d\omega_0/dP<P_{an}$**	**$\pm d\omega_0/dP<P_{an}$**	**$\omega_0>P_{an}$**	**$\omega_0>P_{an}$**	**$d\omega_0/dP>P_{an}$**	**$d\omega_0/dP>P_{an}$**
	(GPa)	(cm^{-1})	(cm^{-1})	(GPa^{-1})	(GPa^{-1})	(cm^{-1})	(cm^{-1})	(GPa^{-1})	(GPa^{-1})
Z1 Uni	2	430	8	-1	6	410	6	2	1

Am4 (ω 996)

Sample	**ω_0**	**$\pm\omega_0$**	**$d\omega/dP$**	**$\pm d\omega/dP$**
	(cm^{-1})	(cm^{-1})	(GPa^{-1})	(GPa^{-1})
Z1 DESY	971	5	5.1	0.8
Z4	997	2	3.2	0.4

Sample	**P_{an}**	**$\omega_0<P_{an}$**	**$\pm\omega_0<P_{an}$**	**$d\omega_0/dP<P_{an}$**	**$\pm d\omega_0/dP<P_{an}$**	**$\omega_0>P_{an}$**	**$\omega_0>P_{an}$**	**$d\omega_0/dP>P_{an}$**	**$d\omega_0/dP>P_{an}$**

	(GPa)	(cm^{-1})	(cm^{-1})	(GPa^{-1})	(GPa^{-1})	(cm^{-1})	(cm^{-1})	(GPa^{-1})	(GPa^{-1})
Z1 Uni	2	1010	13	-12	8	974	5	4.1	0.8
Z3 Uni	4	1028	2	-8	1	995	6	3.2	0.9
Z3 DESY	4	1005	4	-3	2	979	2	5.3	0.3

Declaration

Ich versichere, dass ich die vorliegende Masterarbeit selbstständig vererfasst und keine anderen als die angegebenen Hilfsmittel benutzt habe. Alle stellen, die dem Wortlaut oder dem Sinne nach anderen Texten entnommen sind, wurden unter Angabe der Quellen (einschließlich des World Wide Web und anderer elektronischer Text- und Datensammlungen) und nach den üblichen Regeln des wissenschaftlichen Zitierens nachgewiesen. Dies gilt auch für Zeichnungen, bildliche Darstellungen, Skizzen, Tabellen und dergleichen. Mir ist bewusst, dass wahrheitswidrige Angaben als Täuschungsversuch behandelt werden und dass bei einem Täuschungsverdacht sämtliche Verfahren der Plagiatserkennung angewandt werden können

Felipe Pina Binvignat
Unterschrift

Hamburg den 07.04.2015